REPORT DOCUMENTATION PAGE	*Form Approved* *OMB NO. 0704-0188*

1. AGENCY USE ONLY *(Leave blank)*	2. REPORT DATE June 30, 1996	3. REPORT TYPE AND DATES COVERED Final 1 May 92 - 30 apr 96

4. TITLE AND SUBTITLE DYNAMIC BEHAVIOR OF BRITTLE MATERIALS	5. FUNDING NUMBERS DAAL03-92-G-0192
6. AUTHOR(S) T. J. Ahrens W. G. Knauss G. Ravichandran	
7. PERFORMING ORGANIZATION NAMES(S) AND ADDRESS(ES) California Institute of Technology 1200 E. California Blvd. - MS 105-50 Pasadena, California 91125	8. PERFORMING ORGANIZATION REPORT NUMBER
9. SPONSORING / MONITORING AGENCY NAME(S) AND ADDRESS(ES) U.S. Army Research Office P.O. Box 12211 Research Triangle Park, NC 27709-2211	10. SPONSORING / MONITORING AGENCY REPORT NUMBER ARO 30352.2-MS

11. SUPPLEMENTARY NOTES

The views, opinions and/or findings contained in this report are those of the author(s) and should not be construed as an official Department of the Army position, policy or decision, unless so designated by other documentation.

12a. DISTRIBUTION / AVAILABILITY STATEMENT Approved for public release; distribution unlimited.	12 b. DISTRIBUTION CODE

19960910 019

13. ABSTRACT *(Maximum 200 words)*

The objective of this work aimed at understanding the dynamic response of brittle materials under high rates of loading which are typical of high speed impact and shock generation. Three areas of investigation are covered, namely, (1) the dynamic strength of ceramics in uniaxial compression but under lateral confinement, (2) the propagation of stress waves through fractured but contiguous materials, and (3) shock-induced gas-producing reactions.

The results of these studies indicate: The compression strength of ceramics under high speed impact is systematically and materially increased with progressive lateral constraint or lateral stressing. Wave propagation through fractured solids can be assessed through optical interferometry with high-speed photography. It is suggested that under shock conditions the Rayleigh-Taylor instability of interfacial mixing plays a dominant role in potential chemical processes that are shock induced.

DTIC QUALITY INSPECTED 3

14. SUBJECT TERMS dynamic fracture shock reactions geological materials lateral confinement wave propagation	15. NUMBER IF PAGES 60 16. PRICE CODE

17. SECURITY CLASSIFICATION OR REPORT	18. SECURITY CLASSIFICATION OF THIS PAGE	19. SECURITY CLASSIFICATION OF ABSTRACT	20. LIMITATION OF ABSTRACT
UNCLASSIFIED	UNCLASSIFIED	UNCLASSIFIED	UL

NSN 7540-01-280-5500

Standard Form 298 (Rev. 2-89)
Prescribed by ANSI Std. 239-18

Enclosure 1

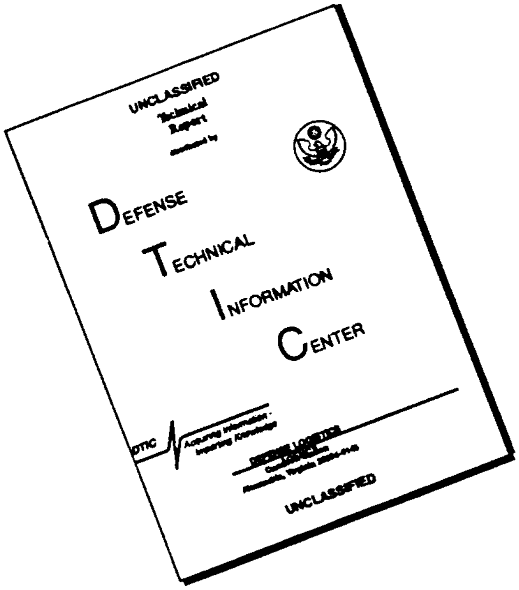

"Dynamic Behavior of Brittle Materials"

Final Report

for the period May 1, 1992 to April 30, 1996

T J. Ahrens
W. G. Knauss
G. Ravichandran

June 1996

U.S. ARMY RESEARCH OFFICE

GRANT NO. DAAL03-92-G-0192

California Institute of Technology
Graduate Aeronautical Laboratories
Pasadena, California 91125

Executive Summary

This report summarizes work conducted at the California Institute of Technology through Research Grant # DAAL03-92-G-0192 under the direction of Professors T.J Ahrens, W. G. Knauss, and G. Ravichandran.

The over-all objective of the work aimed at understanding the dynamic response of brittle materials under high rates of loading, typical of high speed impact conditions. The above participants, along with their students, have facilities that cover different aspects of the common problem setting and thus contributed separate analyses to the program.

The work comprises the three areas of investigation. 1) Dynamic compressive failure of ceramics under multi-axial loading; (2) Wave propagation through fractured solids, and (3) Shock-induced gas-producing reactions.

The first topic deals with the effect of lateral confinement on ceramic strength: Ceramic materials are compressed under high rates of loading typically in one dimensional stress states. A consequence of this loading condition is that shear failures can occur with sections of the specimen breaking off and sliding relative to the main specimen body such that parts of it move normal to the compression axis. This motion is a direct consequence of the unidirectional prescribed stresses.

It is natural to ask whether providing lateral forces to the specimen leads to higher failure values because in this manner the generation of damage within the body is possibly changed. Consequently, the compression failure of ceramic material under impulsive loading (split Hopkinson bar loading) is explored with the specimen encased in different housings to generate varying degrees of lateral (reactive) compression while undergoing high speed axial deformation. It is found that indeed the strength of the ceramic increase with increasing lateral stresses (confinement).

The second problem addresses the fact that when a projectile damages or penetrates a brittle solid under high-speed impact there exists a whole range of fracture phenomena that must be driven by the kinetic energy of the projectile as converted into fractured and/or rubberized material. The primary phenomenon which controls how far penetration occurs is the rate at which energy can be transmitted to the as yet unbroken material. Thus it is very important to understand the nature of wave propagation through broken or fractured material. It was thus the purpose of this study to examine the wave propagation through material that contained cracks but for which the crack surfaces were still in contact.

The problem was studied with the aid of plate specimens; if wave propagation in this simpler geometry was understood, then additional experiments in different geometries could be more readily analyzed. In order to introduce controlled fractures into plates, a material was necessary to choose a solid that allowed relatively easily controlled crack generation. This was accomplished in terms of a low molecular weight Polystyrene, which was characterized with respect to its mechanical properties. High speed photography (200 000 frames per second) and optical interferometry are used to track the propagation of waves through the plate material.

The third topic is concerned with the effect of generating reactions in solids under extremely high pressures as may occur in shock impact. This phenomenon is important in understanding potential phase transitions in impacted solids and its understanding may be essential in formulating numerical algorithms for shock impact problems. This area has been investigated relatively little to date and initial results are presented.

Table of Contents

List of Illustrations

List of Tables

SECTION 1

Dynamic Compressive Failure of Ceramics - Multiaxial Loading

Introduction :

Due to rapid advances in processing technology, high strength ceramics and ceramic composites are being developed with exceptional mechanical properties, and they are being used increasingly in impact related structural applications. In order to design effectively with these materials, it is necessary to develop constitutive models to describe their mechanical behavior and failure modes in these materials under multiaxial dynamic loading conditions. The compressive failure strength of brittle materials has been predicted to increase even under moderate amounts of lateral confinement. This has been observed experimentally in rocks and ceramics under static confinement and quasi-static axial loading conditions; see for example, Heard and Cline (1980), Horii and Nemat-Nasser (1986), Arrowood and Lankford (1987) and Ashby and Sammis (1990). However, the experimental techniques currently available to evaluate the dynamic response of ceramics are essentially limited to either one-dimensional (1-D) stress (e.g., Lankford, 1977) or one-dimensional strain (e.g., Raiser and Clifton, 1993, Grady, 1995) loading conditions. In particular, the influence of confining pressure on the dynamic failure process is not well documented due to the difficulties in recovering damaged ceramic specimens after dynamically loading them. Lankford (1993, 1994) used the Kolsky pressure bar under hydrostatic confining pressure to characterize the compressive behavior of ceramics and ceramic composites, but the failure modes were not reported. New experimental techniques need to be developed which are capable of dynamically loading the brittle specimens over the range of stress states from 1-D stress to 1-D strain. The experimental techniques also should allow for the recovery of the specimen after loading under well defined conditions to facilitate characterization of the failure mode.

In this paper, an experimental technique that is capable of applying dynamic axial compressive loading as well as radial confining pressure to a cylindrical ceramic specimen is presented. The axial loading device is a modified Kolsky pressure bar. Using this technique, it is possible to recover the specimen after subjecting it to a single loading pulse; this feature facilitates further investigation of failure modes and of relation between the microstructure and the macroscopic behavior. The cylindrical ceramic specimen is confined laterally using a shrink fit metal sleeve. Experimental results have been obtained for a glass ceramic material, Macor.

The principles of the experimental technique are presented in Section 2. The quasi-static and dynamic mechanical behavior and characterization of failure mode of Macor under moderate confinement are presented in Section 3. Based on the experimental results, a brittle failure criterion is proposed and discussed in Section 4. The conclusions for the study are presented in Section 5.

Experimental Setup :

The dynamic axial loading device is a modified Kolsky (split Hopkinson) pressure bar with a single loading capability. The cylindrical specimen is confined laterally by a shrink fit metal sleeve. In this section, the modified Kolsky pressure bar is introduced, and the method used for applying lateral confinement is described in detail.

1. Modified Kolsky (Split Hopkinson) Pressure Bar :

Kolsky (split Hopkinson) pressure bar is a well established apparatus commonly utilized in the high-strain-rate testing of materials; see Follansbee (1985). Originally developed by Kolsky (1949), the concept has found widespread applications in testing ductile materials at strain rates up to 10^4 s^{-1}. This technique has been directly applied without any modification to brittle ceramics and ceramic composite materials in dynamic uniaxial compression experiments; see, for example, Lankford (1977). However, the application of this technique for testing brittle materials has serious limitations. As will be discussed below, modifications must be made to the conventional Kolsky pressure bar to avoid repeated loading and to minimize the stress concentrations in the brittle specimen.

The conventional Kolsky pressure bar consists of a striker bar, an incident bar and a transmission bar. A specimen is placed between the incident bar and the transmission bar. When the striker bar impacts the incident bar, an elastic compressive stress pulse, referred to as the incident pulse, is generated and propagates along the incident bar towards the specimen. The pulse duration equals the round-trip time of a longitudinal elastic bar wave in the striker bar. When the incident pulse reaches the specimen, part of the pulse is reflected back in the incident bar due to impedance mismatch at the bar/specimen interface, and the remaining part is transmitted through the specimen into the transmission bar. The strain gages mounted on the bars provide time-resolved measures of the signals in the incident and the transmission bars. Details of this experimental technique can be found elsewhere; see Follansbee (1985). One-dimensional calculations by Kolsky (1949) show that the nominal strain rate $\dot{\varepsilon}$ (t) in the specimen can be calculated using the relation

$$\dot{\varepsilon}(t) = -\frac{2c_o}{l}\varepsilon_r(t) \tag{1}$$

where l is the original length of the specimen, $\varepsilon_r(t)$ is the time-resolved reflected strain measured in the incident bar, and c_o is the longitudinal bar wave speed in the bar material which is given by

$$c_o = \sqrt{\frac{E}{\rho}} \tag{2}$$

where E is the Young's modulus and ρ is the mass density of the bar material. Integration of Eq. (1) with respect to time gives the time-resolved axial strain of the specimen. The nominal axial stress s in the specimen is determined using the equation

$$\sigma(t) = E\frac{A_o}{A_s}\varepsilon_t(t) \tag{3}$$

where A_s is the cross-sectional area of the specimen, and $\varepsilon_t(t)$ is the time-resolved strain in the transmission bar of area A_0. All the foregoing calculations are based on the assumption that the specimen undergoes homogeneous deformation. In the derivation of Eqs. (1) and (3), the incident and transmission bars were assumed to be of the same material and of identical and uniform cross-sectional area.

When brittle materials such as ceramics and ceramic composites are tested in the conventional Kolsky pressure bar, the limitations of the technique must be recognized. In order to obtain reliable and consistent experimental data when testing these materials with the Kolsky bar, appropriate modifications must be incorporated in both the experimental technique and the design of specimen geometry. Many modifications to the Kolsky pressure bar technique and the specimen design have been proposed in the recent literature. For example, shaping of the loading pulse by a thin copper disc, called a pulse shaper, placed at the impact end of the incident bar has been used to prevent the ceramic specimen from failing before equilibrium is attained, and reliable strain data has been obtained during testing by mounting strain gages on the ceramic specimen surface; see Blumenthal *et al.*

(1990), Nemat-Nasser *et al.* (1991) and Ravichandran and Chen (1991). Based on an analysis of one-dimensional elastic wave propagation between the specimen and the elastic bars in Kolsky pressure bar apparatus, Ravichandran and Subhash (1994) established limiting strain rates that can be attained in a ceramic specimen using the Kolsky pressure bar technique.

Using the conventional Kolsky pressure bar technique, it is possible for the specimen to be loaded multiple times due to subsequent wave reflections in the incident bar. In order to characterize the failure mode after a well defined loading history, repeated loading of the specimen is undesirable. Nemat-Nasser *et al.* (1991) developed a momentum trapping technique to achieve the single loading capability. This technique requires extensive modifications of the impact end of the incident bar. In addition, when the specimen strength is high, the momentum trapping device is easily damaged by the high amplitude of the pulses in the incident bar. In the experimental facility used in this study, the transmission bar was made to be shorter than the incident bar (Chen *et al.,* (1995)). With this feature, the shorter transmission bar will act as a momentum trap, thereby moving the transmission bar away from the specimen before a second compressive loading pulse due to reflected tensile pulse in the incident bar reaches the specimen.

The Kolsky pressure bar has traditionally been used to investigate the plastic behavior of metals which are typically softer than the bar material. Under these conditions, the end surfaces of the bars in contact with the specimen remain flat and parallel during the deformation, which results in a nearly uniform stress state in the specimen. However, when a ceramic material is tested, the harder specimen will indent into the end surfaces of the bars during loading, thus causing stress concentrations at the specimen edges. These stress concentrations will result in the premature failure of the specimen and thus make the experimental data invalid; see Chen *et al.*, 1994. In this study, impedance matched tungsten carbide (WC) platens of 12.7 mm in diameter were placed between the specimen and the bars to prevent indentation and minimize the stress concentrations in the specimen.

The experiments were conducted in a modified Kolsky pressure bar facility in the Graduate Aeronautical Laboratories at Caltech. The dimensions of the bars used in this study are 1220 and 580 mm in length for the incident and transmission bars respectively, with a common diameter of 19 mm. The striker bars of 19 mm diameter varied in their lengths from 12.5 to 100 mm to achieve the desired loading pulse duration. All the bars were made of high strength VascoMax (C-350) maraging steel (Rockwell hardness, Rc=55-60). The yield strength of the bars is approximately 2.7 GPa. A pulse shaper which was placed at the impact end of the incident bar was a thin, half hardened copper disc of 0.85 mm in thickness. The diameter of the copper disc was varied to control the rise time of the incident pulse.

2. *Lateral Confinement :*

Confinement of the specimen was achieved by installing a shrink fit metal sleeve on the lateral surface of the cylindrical ceramic specimen as shown in Fig. 1. The inside diameter of the sleeve was slightly smaller than the specimen diameter. To install the sleeve around the specimen, the sleeve was heated to expand the inner diameter and enable the specimen to slide into the sleeve. After the assembly was cooled, the shrinkage of the sleeve provided confinement pressure on the lateral surface of the specimen. The confining pressure (σ_T)produced by the sleeve was estimated by solving an axi-symmetric boundary value problem on the cross-section of a circular elastic (E_1, ν_1) rod (representing the specimen, material 1) inside an elastic-perfectly plastic (E_2, ν_2, σ_{y2}) hollow cylinder (representing the sleeve, material 2) with a misfit at the interface. E_i and ν_i are the Young's modulus and Poisson's ratio of the i^{th} material respectively. σ_{y2} is the yield stress of the sleeve material. The resulting expressions are:

$$\begin{aligned}&\frac{(1-2\nu_2)(1+\nu_2)}{E_2}\sigma_{y2}\left[r_1-\left(2\ln\left(\frac{R}{r_2}\right)+1-\left(\frac{R}{r_2}\right)^2\right)\frac{r_1}{2}\right]+\frac{\left(1-\nu_2^2\right)}{E_2}\sigma_{y2}\frac{R^2}{r_1}\\&+\frac{(1-\nu_1)}{E1}r_1\sigma_{y2}\left[\ln\left(\frac{R}{r_1}\right)+\frac{1}{2}\left(1-\left(\frac{R}{r_2}\right)^2\right)\right]=\frac{\delta}{2}\end{aligned} \tag{4a}$$

$$\sigma_T=\sigma_{y2}\left[\ln\left(\frac{R}{r_1}\right)+\frac{1}{2}\left(1-\left(\frac{R}{r_2}\right)^2\right)\right] \tag{4b}$$

where r_1 is the specimen radius, r_2 is the outer radius of the sleeve, δ is the misfit between the specimen diameter and the sleeve inner diameter, and R is the elastic-plastic boundary radius boundary in the sleeve cross section. The misfit δ can be calculated using the thermal properties of the sleeve material. The confining pressure p can be calculated directly by numerically solving for R from Eq. (4a) and then substituting into (4b). The magnitude of the confining pressure can be varied by using different materials and thickness for the sleeves. The yield strengths of the sleeve materials were experimentally measured using specimens which had been subjected to the same thermal cycle as the sleeves, in order to eliminate any uncertainties due to changes in material properties associated with the thermal cycling. In the case of thin walled sleeves when the sleeve thickness (t) is much smaller than the specimen radius (r_1), the lateral confinement σ_T can be approximated by

$$\sigma_T \cong \frac{\sigma_{y2} t}{r_1}. \qquad (5)$$

The mechanical confinement technique is advantageous since the sleeves are easy to fabricate and no further modifications to the Kolsky pressure bar are required. Also, the plastically deformed sleeve retains the tested specimen allowing examination of the failure mode, even though the brittle specimen itself may have fragmented during the loading. The specimen/sleeve assembly can also be axially loaded in quasi-static loading frames. With the addition of the confining metal sleeve on the specimen in the dynamic experiments, the following formula was used to calculate the axial stress σ_A in the ceramic specimen from the transmitted signal:

$$\sigma_A(t) = E\frac{A_o}{A_s}\left(\varepsilon_t(t) - \varepsilon_{to}(t)\right) \qquad (6)$$

where A_s is the cross-sectional area of the specimen, A_0 is the cross-sectional area of the bar of Young's modulus E, $\varepsilon_t(t)$ is the transmitted signal from the experiment with the confined specimen, and $\varepsilon_{to}(t)$ is the transmitted signal from a test performed on only the sleeve without the specimen. Since the stress state in the sleeve without the specimen is different from the stress state of the sleeve with the specimen, the stress estimated using this approach is an approximation of the actual stress in the specimen. However, the difference in sleeve stress states is not expected to seriously affect the determination of the failure strength since the sleeve material deforms plastically at the strain level where failure strength is measured. On the other hand, the material properties measured at small strains, such as the Young's modulus of the confined specimen, are not considered to be reliable.

3. High Lateral Confinement :

Under axial compressive loading, due to the Poisson's ratio effect, both the ceramic specimen and the metal sleeve expand in the radial direction before the failure of the ceramic specimen. Since the Poisson's ratios of metals are usually higher than those of ceramics, the metal sleeve will expand more than the specimen in the radial direction under axial compression. This excessive lateral expansion in sleeve would cause a relaxation in confining pressure. In fact, the lateral confinement is completely released when

$$(\nu_2 - \nu_1)\varepsilon \geq \frac{\sigma_{y2}}{E_2} \tag{7}$$

where ν_2 and ν_1 are the Poisson's ratios of the sleeve and the specimen materials respectively, ε is the axial strain which is the same for both the specimen and the sleeve during axial loading, σ_{y2} and E_2 are the yield stress and the Young's modulus of the sleeve material.

In the axial loading process, the lateral confinement provided by the metal sleeve decreases as the axial strain is increased. The relaxation will occur more rapidly when the sleeve begins to deform plastically, hence ν_2 approaches 0.5. In order to investigate issues such as the brittle/ductile transition in brittle materials, it is desirable to not only achieve, but also maintain high confining pressures during the process of axial loading.

A second shrink-fit metal sleeve was introduced to eliminate the loss of confining pressure during axial deformation of the confined specimen. The second sleeve was machined with chamfered ends. Its length was the same as the specimen at its inside diameter and symmetrically decreased radially. The pressure from the shrink fit of the second sleeve maintained the confining pressure on the ceramic specimen generated by the first sleeve. The tapered shape ensures that the second sleeve would not be affected by the axial compression and the Poisson's ratio effect at small axial strains on the order of 1-3%. The axial stress in the ceramic specimen can be estimated by Eq. (6). In this case, the sleeve-only experiments involves the assembled double sleeve without the ceramic specimen in the assembly. The confining pressure on the specimen was also estimated using Eqs. (4a) and (4b). The outer sleeve was assembled in such a way to generate little or no confinement on the specimen compared to that generated by the inner sleeve. However, it is essential for maintaining the lateral pressure on the specimen generated by the first sleeve during axial loading.

Dynamic experiments were performed on Macor specimens confined by the double sleeves using the modified Kolsky pressure bar. The cylindrical specimens were 6.35 mm in diameter and 9.50 mm in length. The inside diameter of the first sleeve was machined to be 0.025 mm less than the specimen diameter, and the outside diameter was 9.525 mm. The inside diameter of the second sleeve was 9.500 mm with the outside diameter being 15.875 mm. The chamfer on the second sleeve was 30 degrees from the specimen end faces. The two concentric sleeves on a given specimen were made of the same material. Since a tapered second sleeve is used, it was not possible to mount a strain gage on the specimen surface to monitor the axial stain as was done with the single sleeved specimens. If dynamic experiments have to be performed on hard ceramic materials confined by the concentric double sleeves using the Kolsky pressure bar, new techniques must be developed to reliably measure the axial strain during loading. However, Macor is a relatively soft ceramic material as demonstrated by the earlier experimental results (Ravichandran and Chen (1991)), and therefore, it is feasible to use the reflected signal in the incident bar to estimate the axial strain rate in the specimen using Eq. (1). In these high confinement experiments, a 50 mm long maraging steel striker bar was used. The striker bar velocity was approximately 40 m/s.

4. Materials :

The material used in this investigation is a commercially available machinable glass ceramic composite commonly known as Macor; see Corning (1992) and Cai et al. (1994). Macor is a white glass ceramic composite comprised of a fluorophlogopite mica phase (55%) interspersed in a borosilicate glass matrix (45%). The microstructure consists of a network of randomly oriented interlocking 1-2 μm thick mica flakes that are approximately 10 μm in planar dimension parallel to the cleavage basal plane. Some of the relevant physical properties of Macor (Corning, 1992) are listed in Table 1.

The Macor specimens used in this investigation for single sleeved experiments were 8.10 mm in diameter and 8.25 mm in length. The Macor specimens were ground cylindrical to within 0.005 mm on the lateral surface with the two end faces parallel to within 0.005 mm. Macor was chosen for the present investigation because of its low moduli and low compressive strength as listed in Table 1, while possessing the same physical attributes of a brittle ceramic material. Hence, Macor was expected to serve as a model ceramic material for the present investigation.

Five different sleeve materials were used to apply varying amounts of confining pressure. The sleeve materials and their quasi-static yield strengths are listed in Table 2. The quasi-static yield strengths in Table 2 were measured by mechanical tests with the sleeve materials which had been heated and cooled under the same conditions as for the sleeve/specimen assembly process described below.

The sleeves had the same length as the specimens, with an average wall thickness of 0.73 mm. The mismatch between the sleeve inside diameter and the specimen diameter was chosen to be at least 0.025 mm (i.e., d=0.025 mm, see Fig. 1). For this mismatch, the hoop stress in the sleeve always reaches the yield strength of the sleeve material, and Eq. (5) is a good approximation of the lateral confinement generated by the single sleeve. To assemble the sleeves and the specimens, the copper and brass sleeves were heated to a temperature of ~ 450 ^{0}C, whereas the steel sleeves were heated to ~ 850 ^{0}C for 40 seconds. The PMMA sleeve was placed in boiling water before assembly. After the sleeve was installed on the specimen, the end surfaces of the assembly were polished to a 1 μm surface finish using diamond paste to remove surface damage from grinding and sleeve installation. On each assembly, an axial strain gage was mounted on the outer surface of the sleeve. Olsson and Forrestal (1994) have used a similar confining sleeve design in their investigation of the effect of confinement on the failure behavior of concrete.

5. Quasi-Static Experiments :

To compare with dynamic experimental results, quasi-static experiments were performed on Macor. A hydraulically driven Materials Test System (MTS) was used to apply an axial compressive load. A load cell (MTS axial-torsional load transducer, model 662.10A-08) in the MTS crosshead recorded the axial load data. The axial strain gage mounted on the outer surface of the confining sleeve was used to accurately monitor the axial deformation of the specimen. Furthermore, a high sensitivity LVDT was mounted on the loading grips across the specimen to continuously monitor the deformation of the specimen in case the strain gage failed or became unreliable at large strains. The MTS actuator moved at a constant velocity in the displacement control mode during the experiments. Varying strain rates were obtained by varying the actuator velocity through the MTS controller. The load, axial strain signals from the strain gage and the high sensitivity LVDT were recorded using a Nicolet 440 digital oscilloscope.

The total axial loading data measured by the load cell contained the contributions from both the specimen and sleeve. In order to obtain the axial stress data from the ceramic specimen, a sleeve-only test was performed immediately after each experiment with identical experimental parameters. The axial stress σ_A in the ceramic specimen was computed using the equation:

$$\sigma_A = \frac{(F_T - F_o)}{A_s} \tag{8}$$

where F_T and F_o are the axial load measured by the load cell in experiments with the confined specimen and with the sleeve only, respectively; and A_s is the cross-sectional area of the ceramic specimen. This is analogous to Eq. (6) for the dynamic experiments.

Experimental Results :

1. Constitutive Behavior of Confined Macor :

Quasi-Static Behavior

Figure 2 shows the typical stress-strain curves from experiments on Macor without confinement and two specimens with moderate confining pressure of 47 and 88 MPa. The nearly linear stress-strain behavior of the unconfined specimen prior to failure is typical of brittle materials under quasi-static uniaxial compression. The specimen fails catastrophically at the peak stress defined as the compressive strength. When lateral confinement was applied, there is a clear change in the stress-strain behavior of the material. Inspection of Fig. 2 indicates that the peak stress of the material is seen to increase with lateral confinement. Instead of catastrophic failure, after the peak stress was attained, there was an unstable region of the stress-strain curves for the confined specimens. The load carrying capacity of these specimens decreased as the strain increased further as shown by the solid and dotted curves in Fig. 2. After the unstable region, the load carrying capability was essentially independent of the axial strain, which also increased with increasing confining pressure. The variation of the compressive strength with the amplitude of lateral confinement is plotted in Fig. 3. For the unconfined case, the average compressive strength obtained from 5 specimens was 435 MPa on the Macor material used in this research, although the strength quoted by the manufacturer was 345 MPa as listed in Table 1. As the lateral confinement was increased from 0 to 88 MPa, the compressive strength increased monotonically from 435 MPa to 485 MPa.

Dynamic Behavior

Figure 4 shows typical stress-strain curves from dynamic experiments on Macor without confinement and two specimens with lateral confinement (σ_T) of 47 and 230 MPa. The axial strain was determined from the signal measured by the strain gage on the specimen except for the case of 230 MPa confinement where strain was determined by integrating Eq. (1), whereas the stress was calculated from the transmission bar signals using Eq. (6). As shown in Fig. 4, the stress-strain relation for the unconfined specimen was nearly linear. The Young's modulus was determined to be 63 GPa which is close to the value given by the manufacturer listed in Table 1. When lateral confinement was applied on the specimen, the stress-strain behavior appeared to be quite different from the behavior observed in the dynamic, uniaxial stress case. The initial part of the stress-strain curve of the specimen with σ_T=47 MPa was nearly linear with the apparent modulus being higher than the Young's modulus of the unconfined specimen as shown in Fig. 4. For the reasons discussed earlier, the value of the modulus at small strain levels is not considered to be reliable since Eq. (6) was used in the data reduction. After the axial stress reaches about 350 MPa, which corresponds to an axial strain of 0.44%, the tangent modulus decreased to ~22 GPa and further decreased as the axial strain increased. Investigation of the strain history shown in Fig. 5, revealed that after the axial strain reached ~0.44%, the strain rate as indicated by the slope of the curve, increased drastically from 200 to 2800 s^{-1}. The shape of the stress-strain curve for the confined specimen under dynamic loading shown in Fig. 4 appears to be similar to a work-hardening ductile material instead of a brittle ceramic.

With the presence of lateral confinement, the stress-strain behavior of Macor cannot be assumed to be linear until failure which characterizes most brittle ceramic materials in uniaxial compression experiments. The stress-strain behavior following the peak stress is not as clear in Fig. 4 as compared to the quasi-static behavior shown in Fig. 2 due to the failure of the axial specimen strain gages at strains of ~3% in the single sleeved dynamic experiments. The transmission bar signal shown in Fig 5, however, provides a measure of the variation of the load carrying capacity of the specimen as a function of time. Inspection of the transmitted signals in Fig. 6 indicates that the behavior of the moderately confined Macor specimen under dynamic axial loading was similar to the corresponding behavior under quasi-static loading. After the peak stress was attained, the axial loading carrying capacity of the specimen dropped suddenly to a lower stress level, and then remained essentially constant until unloading.

The specimen confined using double 303 stainless steel sleeves ($\sigma_T = 230$ MPa) behaved differently in comparison to the unconfined and moderately confined specimens. During the loading process, the axial strain increased with loading until the strain reached 2%. As the axial strain was increased further from 2%, the axial stress in the specimen remained nearly constant until unloading. There was no apparent unstable portion in the stress-strain curve comparable to that observed in the cases with lower lateral confinement. The specimen exhibited elastic-perfectly plastic like stress-strain behavior when confined by the stainless steel sleeves. The average stress measured from the plateau of the stress-strain curve was approximately 1.35 GPa. The magnitude of the confining pressure generated by the stainless steel sleeves was 17 % of this plateau stress. The permanent strain measured on the recovered specimen was approximately 2% which compares well with the permanent residual strain indicated by the stress-strain curve in Fig. 2.

The stress value at a peak point in Fig. 4 is defined as the dynamic compressive strength of Macor, σ_c, under given lateral confinement at corresponding strain rate. The variation of compressive strength, σ_c, as a function of lateral confinement, σ_T, is plotted in Fig. 6. It is apparent from Fig. 6 that the compressive strength increased from 0.45 GPa to approximately 1.35 GPa as the lateral confining pressure was increased from zero to 230 MPa.

2. *Failure Mode Characterization :*

Failure Mode Under Quasi-Static Loading

Figure 7 shows the top view, the bottom view and the axial cross-sectional view of 4 recovered specimens. The specimens without confinement and with a PMMA confining sleeve fragmented when load reached compressive strength during the quasi-static experiments. The recovered specimens shown in Fig. 7 from left to right, are those confined by a 6061 aluminum sleeve (σ_T=26 MPa), a brass sleeve (σ_T=47 MPa), a 2024 aluminum sleeve (σ_T=50 MPa) and a 303 stainless steel sleeve (σ_T=88 MPa). The advantage of using plastically deformed sleeves to confine the ceramic specimens for failure investigation is clearly illustrated in Fig. 7, where the fractured specimens are retained by the sleeves. Inspection of the top and bottom views indicates that the initially circular cross-sections of the specimens became irregular in shape, which implies that the deformation of the specimen was no longer homogeneous after damage initiation. In each of the recovered specimens, there was a cone shaped region with its base sitting at one of the flat faces of the specimen. Within the conical region, the crack density was much lower than that observed outside the cone. The conical surface formed a fault, in which the material was granulated. This indicates a severe sliding motion across the fault during the later stages of deformation. The resistance of the material to sliding thus may correspond to the stress level of the nearly horizontal region of the stress-strain curve in Fig. 2. Since the resistance to the sliding was much lower than the compressive strength of the material, the faults were expected to form when the compressive strength in the specimen was reached.

Failure Mode Under Dynamic Loading

The failure modes of the dynamically loaded specimens were similar to those of the quasi-statically loaded specimens shown in Fig. 7. The specimen tested without confinement was fragmented completely, even though it was loaded under the identical experimental conditions as the confined specimens. With lateral confinement, the tested and thus damaged specimens were retained by the plastically deformed sleeves. The visible crack density on the specimen end faces decreased with increasing confinement pressure. The propensity for crack growth appeared to be suppressed by the lateral confinement pressure. It was also observed that the initially circular cross-sections of the specimens became irregularly shaped, indicating that deformation was not homogeneous after damage initiation. The recovered specimens were sectioned with a low speed diamond saw to reveal a surface parallel to the loading axis. A conical region was found in each of the recovered specimens, similar to those observed in the quasi-statically deformed specimens shown in Fig. 7. The cones in the specimens recovered from dynamic experiments were almost right cones: the apex of the cone was located very close to the specimen center. The conical faults in the dynamically loaded specimens were more regular then the cone shape from a quasi-statically loaded specimen. Figure 8 is an illustration of typical axial cross section. Inspection of Fig. 8 indicates that the conical surface divides the specimen into two regions. Inside the cone the crack density was very low, whereas outside the cone the material was cracked extensively. Typically, the fragment sizes in the region outside the cone were larger than the comminuted fragments of the unconfined specimen. The crack density outside the conical region decreased with increasing confining pressure. Furthermore, a thin annular region of granulated material was observed on the end of the confined specimen where the base of the cone was located, indicating a very high local crack density. In fact, the annular region is a cross-section of a layer of ceramic rubble formed on the conical surface, which implies that there was severe sliding motion across the conical fault in the deformation process.

The recovered double-sleeved specimens were also sectioned to reveal a surface parallel to the loading axis. A conical fault was again observed in the double brass sleeved (σ_T=120 MPa) specimen, similar to the faults found in the Macor specimens confined by thin-walled sleeves as shown in Fig. 8. However, in the axial cross section of the double stainless steel sleeved (σ_T=230 MPa) specimen, no visible cracks were observed under the optical microscope even at the stress concentrated corners. The observations that the specimen was deformed permanently and no cracks were created during deformation indicate that inelastic deformation must have occurred in the specimen. The occurrence of inelastic behavior was also confirmed by the stress-strain curve shown in Fig. 4. Therefore, a failure mode transition from brittle to ductile is considered to occur in Macor when the lateral confinement is between 120 and 230 MPa. This is believed to be the first time a ceramic specimen with permanent deformation and no visible damage has been recovered from a controlled laboratory experiment at room temperature.

The dimensions of each specimen were measured before and after the dynamic experiment. The average permanent axial strain was 7.5% on a recovered specimen with confinement which was loaded by a projectile of 100 mm in length. A 303 stainless steel confined specimen was loaded by a 50 mm long projectile, and the permanent axial strain was measured as 2.1%. In comparison, failure strains of unconfined specimens were typically less than 1%. In the case of the stainless steel sleeved specimen, there was a cone inside the recovered specimen as will be discussed later, but the permanent strain was only 2.1 %, which indicates that the permanent strain was accumulated mainly after the formation of the conical fault when the specimen suffered a drop in loading carrying capacity at axial strains of 2-3%. The axial stress remained nearly constant after the drop as the axial strain further increased to accumulate most of the permanent strain. If the axial load was terminated just after the compressive strength was reached in the specimen, the permanent axial strain level would be much lower. This was the case with the stainless steel sleeved specimen. Therefore, the majority of the permanent strain was accumulated in the post-failure region by the sliding of the material across the conical fault.

Formation of the Conical Fault

Conical faults were observed in all the laterally confined specimens recovered from both quasi-static and dynamic experiments. The formation of this fault appears to be the key factor which determines the compressive strength and dominates the mechanical behavior of the specimen after the compressive strength is reached. Therefore, it is necessary to understand the process of the fault formation along with important parameters associated with the process. In order to investigate the process of conical fault formation, the axial loading was terminated at various strains just after the peak stress was attained. This level of load control cannot be achieved quasi-statically on the MTS since there is elastic strain energy stored in various parts of the load frame. However, in the modified Kolsky pressure bar, with the single loading feature and the precise control over the shape, magnitude, and duration of the loading pulse by the pulse shaper, the striker bar velocity and the striker bar length, respectively, it is feasible to terminate the axial loading at various stages after the peak, and therefore it is possible to study the process of the conical fault formation in detail.

Experiments were conducted with a 26 mm long striker bar on specimens confined laterally at σ_T=47 and 88 MPa. The recovered specimens were again cut to reveal a cross-section parallel to the loading axis. Various stages of the conical fault formation process were revealed by inspection of the crack/fault patterns on the cross sections. Figure 9 shows schematic views of four typical cross sections revealing the formation process of the conical fault. Since the cracks were very thin just after initiation, it was difficult to identify crack patterns in the original photographs. Therefore, schematic drawings were traced from the original photographs. The cross section in Fig. 9(a), corresponding to 1% of axial stain, shows almost no damage in the specimen except for small cracks initiating from the four corners. Figure 9(b) shows that cracks have propagated from the corners into the specimen, and intersect near the middle at an axial strain of 1.7%. A pair of the cracks from one end of the specimen stopped propagating at the intersection, whereas the pair from the opposite side continued to propagate until intersecting each other to form a conical fault as shown in Fig. 9(c) at 2% of strain. No rubble was observed between the just-formed fault surfaces. With continued loading after the formation of the fault, granulated material was found within the fault as shown in Fig. 9(d) at 8% of axial strain, which indicated that there was substantial sliding motion across the fault after its formation. The resistance to the sliding motion in the rubble layer apparently does not depend on the relative positions of the opposite sides across the fault, accounting for the perfectly-plastic-like behavior of the specimen.

3. *Dynamic Shear Behavior of Pulverized Ceramic :*

The post-failure strength of the confined Macor specimens can be determined from the nearly horizontal portion of the stress-strain curve at large strains as shown in Figs. 2 and 5. It was also suggested from the discussions on the failure mode that the nearly flat portion of the stress-strain curve is related to the sliding motion across the conical fault. The shear stress and strain rate in the rubble layer in the conical fault may be estimated using the post-failure strength data and the fault geometry as illustrated in Fig. 10. The normal stress σ^n and shear stress τ in the rubble layer of thickness h can be computed by

$$\sigma^n = \sigma_A \cos^2\theta + \sigma_T \sin^2\theta \tag{9a}$$

$$\tau = \frac{1}{2}(\sigma_A - \sigma_T)\sin 2\theta \tag{9b}$$

where σ_A and σ_T are the axial stress and the lateral confining pressure on the specimen, respectively, 2θ is the apex angle of the cone. The shear strain rate can be estimated by

$$\dot{\gamma} = \frac{(v_1 - v_2)}{h}\cos\theta \tag{10}$$

where v_1 and v_2 are the particle velocities at the two end faces of the specimen as illustrated in Fig. 10. Since the axial strain rate of a specimen of length l is $\dot{\varepsilon} = \frac{(v_1 - v_2)}{l}$, the shear strain rate can be related to axial strain rate by

$$\dot{\gamma} = \dot{\varepsilon}\left(\frac{l}{h}\right)\cos\theta. \tag{11}$$

In an experiment, l is measured before loading the specimen, σ_T is estimated using Eqs. 4 or 5, σ_A and $\dot{\varepsilon}$ are measured in the experiment after the unstable behavior as described in the previous sections regarding the constitutive behavior, h and θ are measured on the recovered specimen after the loading. Therefore, the shear stress and the shear strain rate in the conical layer of ceramic rubble under steady state sliding can be experimentally determined through Eqs. (9b) and (11).

In order to make a meaningful estimation of the shear stress and the shear strain rate in the ceramic rubble using Eqns. (9b) and (11), the shape of the conical fault should be relatively well defined. The conical faults in the recovered specimens from dynamic experiments have relatively more regular shaped than those from quasi-static experiments. Therefore, estimations were only made based on the dynamic experimental results.

The average value of the apex angle 2θ was measured to be 57.22^0 from the recovered Macor specimens with the geometry described earlier in Section 3.1. The average thickness (h) of the conical rubble layer was measured to be 150 μm. The initial specimen length l was 8.25 mm. The axial strain rate at the post-failure stage (where sliding across the fault was believed to be the dominant mechanism) was recorded to be 2800 s^{-1} as shown in Fig. 5. Based on these experimental data, the shear strain rate in the rubble layer is calculated using Eq. (11) to be $\dot{\gamma} = 1.35 \times 10^5 s^{-1}$.

Table 3 lists the estimated confining pressure σ_T, the average post-failure strength σ_A and the shear stress τ calculated using Eq. (9b), for the Macor specimens confined by copper, aluminum, and brass sleeves where granulated faults were observed. The ratios of shear stress to axial stress τ/σ_A and shear stress to mean pressure τ/p for the various cases are also tabulated in Table 3, where $p = (\sigma_A + 2\sigma_T)/3$. It is clear from Table 3 that both ratios τ/σ_A and τ/p decrease as the confinement pressure increases. One possible reason for the reduction in the ratios is that the grain size in the rubble layer reduces as the lateral confinement σ_T increases. Klopp and Shockey (1991) and Sairam and Clifton (1994) obtained the ratio τ/p to have a limiting value of approximately 0.2 for fine ceramic powder (average particle size ~0.4 μm) using a pressure-shear plate impact technique.

The Failure Criterion :

1. Mohr-Coulomb Failure Criterion :

The nearly linear dependence of the compressive strength on the confining pressure shown in Figs. 3 and 6 suggests that the material's brittle failure behavior (axial splitting of brittle faulting) may be described by the Mohr-Coulomb failure criterion

$$|\tau| + \alpha p = \tau_o \qquad (12)$$

where $p = -\frac{1}{3}\sigma_{kk} = -\frac{1}{3}(\sigma_A + 2\sigma_T)$

and $|\tau| = \frac{1}{2}|\sigma_A - \sigma_T|$.

$|\tau|$ is the absolute value of shear strength, p is the hydrostatic or the hydrodynamic pressure, τ_0 is the shear strength of the material without any pressure (pure shear), and α, referred to as the internal friction coefficient, is the proportionality coefficient between $|\tau|$ and p. Mohr-Coulomb failure criterion has been used extensively in rock mechanics (e.g., Jaeger and Cook, 1979). The experimental dynamic compressive strength data in Fig. 6 can be plotted as a failure surface in the p-τ plane as shown in Fig. 11. The values of τ_0 and α were determined to be 0.11 GPa and 0.74, respectively. It is clear that Mohr-Coulomb failure criterion is suitable to describe the brittle failure behavior of Macor.

2. *Rationale for the Failure Criterion :*

As was demonstrated by the results earlier in section 3, when a brittle solid is axially loaded in compression to failure either quasi-statically or dynamically, crack initiation, propagation, and interaction are considered to be the dominant failure mechanisms if the lateral confinement is not sufficient to attain the brittle to ductile transition in the failure mode. The brittle compressive failure mode was observed to be either axial splitting under uniaxial stress or faulting under moderate confinement pressure. The sources of crack initiation in brittle materials have been simplified to two fundamental types: (1) a spherical cavity or (2) a sharp microcrack; see Ashby and Sammis, 1990. Theoretical investigations based on fracture mechanics have been performed on these two simplified cases (e.g., Horii and Nemat-Nasser, 1986, Ashby and Sammis, 1990). A typical picture of a microscopic sliding crack is shown in Fig. 12. New cracks initiate from the two ends of an existing crack when the opposite crack surfaces slide against each other under loading. The analytical results showed that a brittle material will fail under multiaxial compression when

$$\sigma_1 = c\sigma_3 - \sigma_o \tag{13}$$

where σ_1 is the axial stress which is equivalent to σ_A, c is a material constant, σ_3 is the transverse stress which is equivalent to σ_T, and σ_o is the unconfined compressive strength. This failure criterion has been validated by experiments conducted under quasi-static loading conditions on brittle materials (Ashby and Sammis, 1990). Furthermore, it was demonstrated that at the initiation of the crack propagation, c and σ_o can be expressed as

$$c = \frac{\left(1+\mu^2\right)^{1/2} + \mu}{\left(1+\mu^2\right)^{1/2} - \mu} \tag{14}$$

and

$$\sigma_o = \frac{\sqrt{3}}{\left[\left(1+\mu^2\right)^{1/2} - \mu\right]} \frac{K_{Ic}}{\sqrt{\pi a}} \tag{15}$$

where μ is the coefficient of friction acting across the crack surfaces, K_{Ic} is the fracture toughness of the material, and 2a is the length of the original inclined crack.

Equation (13) can be compared directly to the Mohr-Coulomb failure criterion (Eq. (12)), assuming $\sigma_2=\sigma_3=\sigma_T$ and using

$$\alpha = \frac{3(1-c)}{2(2+c)} \tag{16}$$

and $$\tau_o = -\frac{3\sigma_o}{2(2+c)}. \tag{17}$$

The combination of (14) and (16) yields

$$\alpha = \frac{3\mu}{3\left(1+\mu^2\right)^{1/2} - \mu} \tag{18}$$

which indicates that based on the analysis on the simplified sliding crack model for brittle failure, the slope of the failure surface depends solely on the friction coefficient μ of the sliding crack surfaces. If μ is independent of the applied pressure and the imposed strain rate on the material, then the slope of the failure surface will be the same for various pressures and strain rates. It should be noted that the friction is acting on the sliding surfaces of a microcrack, and may differ from the coefficient of friction measured using macroscopic methods.

It is well known that the unconfined compressive strength σ_0 for ceramics is strain-rate dependent, e.g., see Lankford (1977) and Ravichandran and Subhash (1995). Equation (15) indicates that the compressive strength σ_0 depends on the fracture toughness K_{Ic}, the coefficient of friction μ and the initial flaw size 2a. The pure shear strength τ_0 in the Mohr-Coulomb criterion is related to the compressive strength σ_0 and the coefficient of friction μ by Eqns. (17) and (14). Therefore, the shear strength term in the in Eq. (12) depends on both the strain-rate and the friction. However, the frictional behavior of ceramics at a microscopic scale is not well understood.

The physical significance of Eq. (12) may be described as follows. In the brittle failure process, the inelastic deformation of the specimen is accommodated by crack propagation and interaction. Crack surfaces are expected to be sliding against each other in the deformation process as illustrated by Fig. 12. Friction exists on the sliding surfaces which resists the sliding motion. The magnitude of the friction depends proportionally on the pressure acting on the surfaces. The bulk material behavior of the material is expected to reflect the averaged microscopic behavior. Therefore, the shear bearing capability of the bulk material is expected to increase with increasing pressure acting on the specimen. The higher the pressure, the higher the frictional resistance on the microcracks, hence the higher the shear strength of the bulk material. Equation (12) is the simplest phenomenological expression describing this physical picture. The sliding crack model shown in Fig. 12 describes a typical microscopic feature of brittle failure. This is demonstrated by the consistency of the failure criterion derived from the simple model using fracture mechanics with the experimentally obtained Mohr-Coulomb criterion as shown above by the equivalence of Eq. (13) to Eq. (12).

3. *Rationale for Ductility in Ceramics at High Confining Pressures :*

It should be noted that both the experimentally obtained Mohr-Coulomb failure criterion, Eq. (12), and the analytically obtained failure criterion, Eq. (13), describe the material behavior of brittle failure. Brittle failure prevails for ceramic materials under axial compression with little or no lateral confinement as demonstrated by the experimental results on Macor presented above. When the lateral confining pressure reached 230 MPa, a transition in deformation mode in Macor from brittle to ductile was observed. Heard and Cline (1980) observed a brittle-ductile transition in many engineering ceramics in their quasi-static tri-axial experiments at high confining pressures. Under dynamic loading conditions, a similar change in the failure mode was observed in Macor. Under high confining pressures, the pre-existing microcracks will be closed although the stress concentrations at the crack tips still exist. When the applied compressive stresses are sufficiently high, defects (e.g., dislocations, twins, kink pairs) may be generated at the stress concentrated crack tips since the cracks cannot propagate to relax the high stresses at the tips. The deformation of the ceramic material under high confining pressure is thus expected to be governed by a plastic flow criterion, for example such as the von Mises or the Tresca. In the p-τ plane, such a criterion is represented by a horizontal line. Based on the available failure strength data obtained under high pressures, such a failure surface represented by a nearly horizontal line in the p-τ plane has been constructed, see Chen (1995). The ductile to brittle transition in brittle materials has been analyzed by Horii and Nemat-Nasser (1986). However, the mechanisms for the plastic deformation in brittle materials under high pressures are not well understood at the present time due to the paucity of experimental data and microstructural characterization.

Conclusions :

An experimental technique has been developed for imposing controlled lateral confinement on specimens subjected to dynamic uniaxial compression. The axial compressive loading was applied using the Kolsky pressure bar modified to apply a single loading pulse. The cylindrical specimens were confined laterally by shrink fit metal sleeves. During an experiment with a sleeve confined specimen, the specimen is subjected to a single, known loading pulse. The failure mode can thus be characterized in the recovered specimen. The experiments indicated that for moderate confining pressures (up to 230 MPa), the compressive failure strength of a glass ceramic composite, Macor, increases linearly with increasing confining pressure under both quasi-static and dynamic loading conditions. Examination of recovered specimens showed that under confining pressure the failure mode changed considerably from complete fragmentation under the condition of uniaxial stress to localized brittle faulting in specimens under moderate confinement. Conical faults initiated from the corners, and penetrated into the specimens. After the formation of the faults, further axial deformation of specimens was accommodated by the sliding motion of the material across the faults. Ductile behavior was observed in Macor at a confining pressure of 230 MPa. This is believed to be the first time a ceramic specimen with ductile behavior has been recovered from a controlled laboratory experiment at room temperature. The Mohr-Coulomb criterion fits the strength data well, which also agrees with the prediction of the analytical results of a micromechanical brittle failure model.

TABLES

Table 1. Physical Properties of the Glass Ceramic, Macor

Density, ρ	2520 kg/m^3
Young's Modulus, E	64.1 GPa
Shear Modulus, G	25.4 GPa
Poisson's Ratio, ν	0.26
Quasi-Static Compressive Strength	345 MPa

Table 2 Sleeve Materials and Corresponding Estimated Confinement Pressures

Sleeve Material	Yield Stress (MPa)	Confining Pressure (MPa)
PMMA	55	10
Copper	120	22
Al6061-T6	144	26
Brass*	261	47
Al2024-T3	277	50
Stainless Steel 303	488	88

*Free cutting brass rod (S.A.E. Standard No. 72)

Table 3. Shear Stress in the Pulverized Layer along the Conical Faults

Sleeve Material	σ_T, MPa	σ_A, MPa	τ, MPa	τ/σ_A	τ/p
Copper	22	140	50	0.357	0.815
Al 6061	26	153	53	0.346	0.776
Brass	47	176	54	0.307	0.600
Double Brass	120	420	126	0.300	0.573

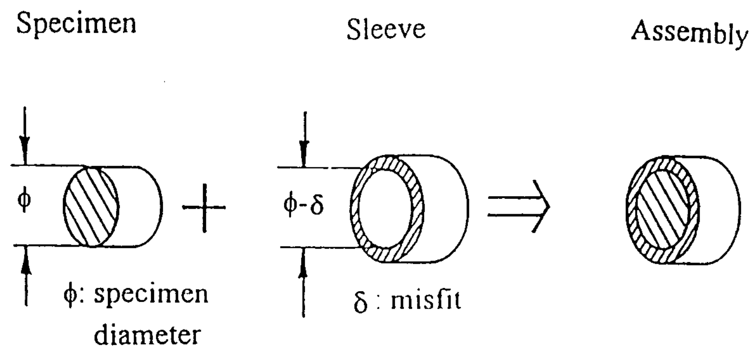

Fig. 1. Schematic illustration of the shrink-fit metal sleeve used to confine the ceramic specimen.

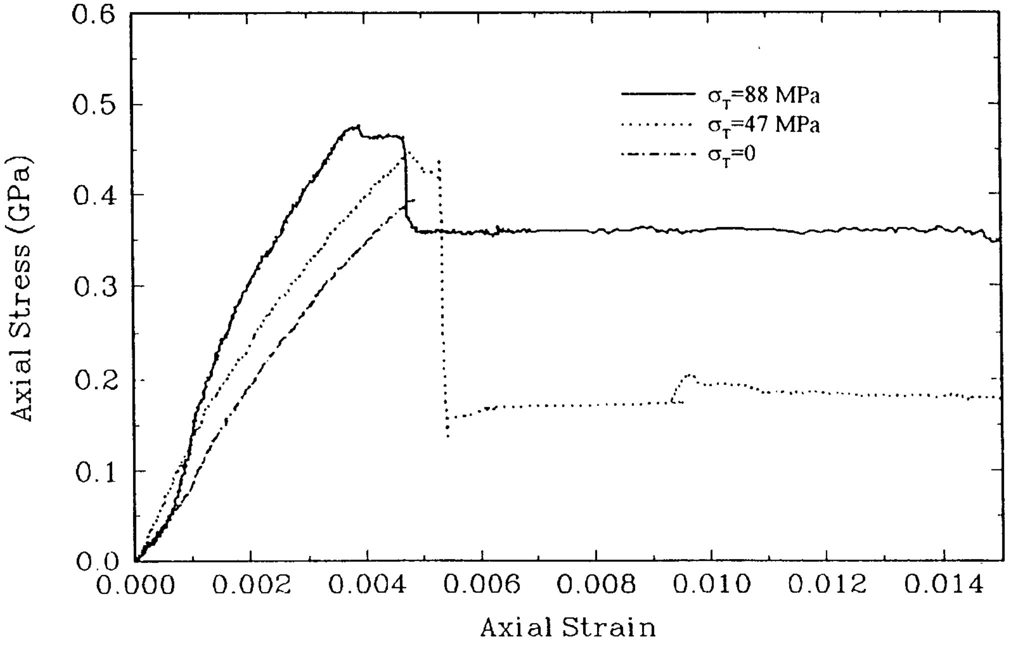

Fig. 2. Typical quasi-static stress-strain curves of Macor under various confinement.

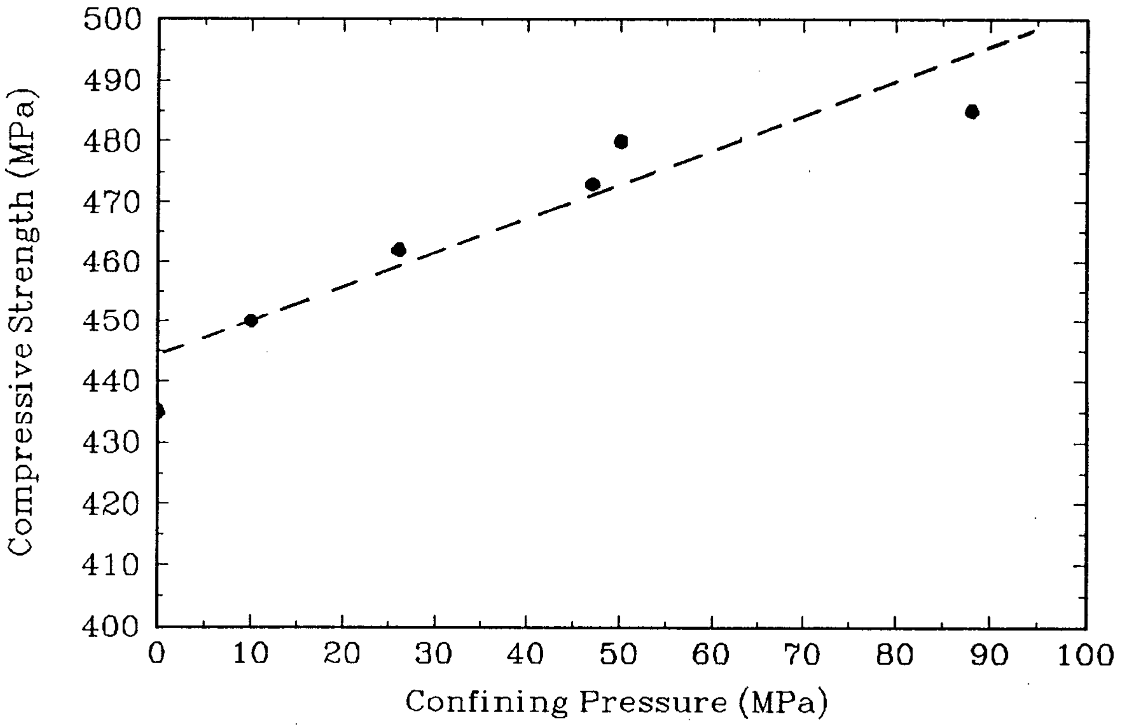

Fig. 3. Variation of quasi-static compressive strength of Macor with confinement.

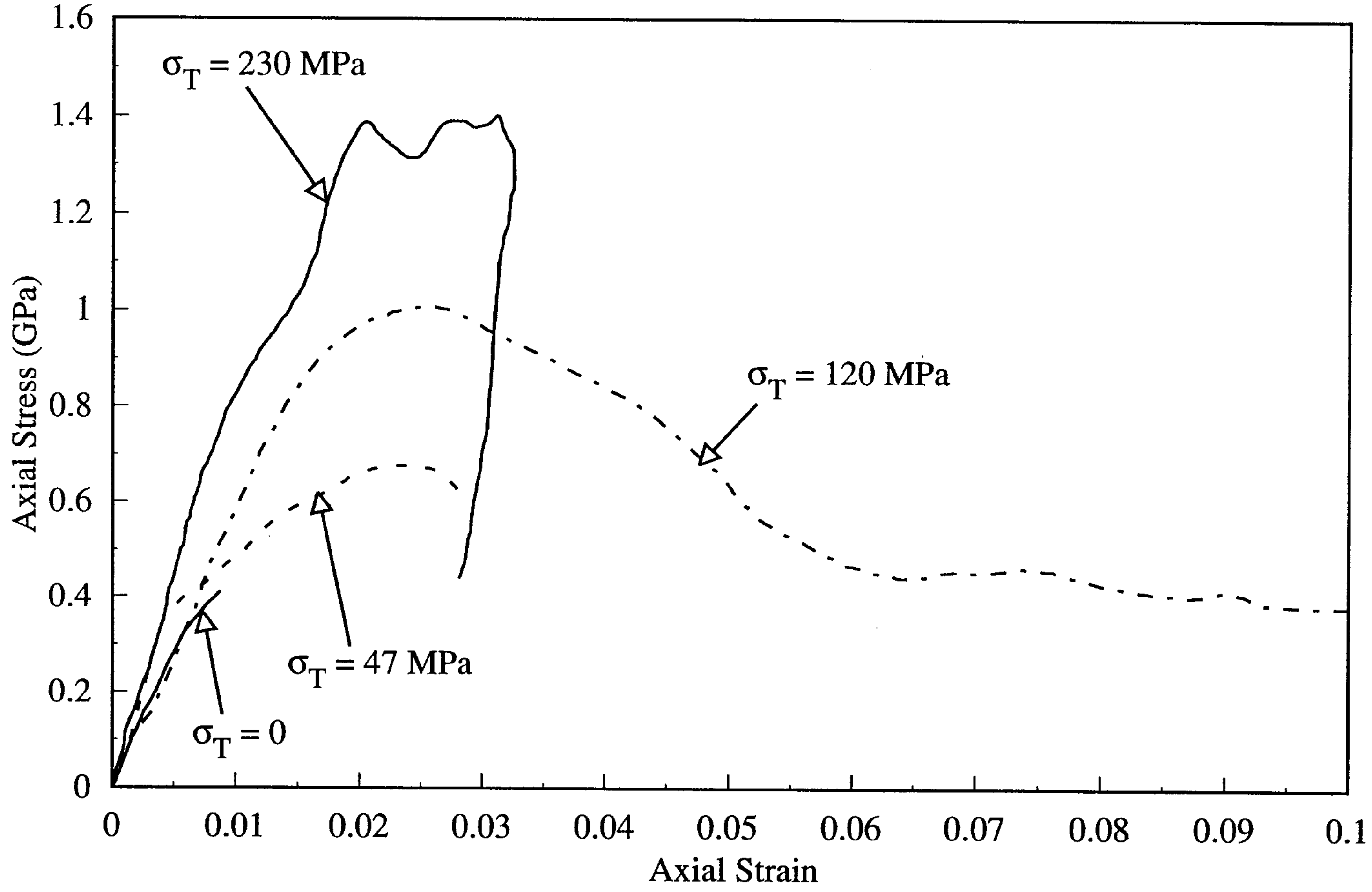

Fig.4.Typical dynamic stress-strain curves of Macor under various levels of lateral confinemnet, $\sigma_T = 0, 47, 120$ and 230 MPa.

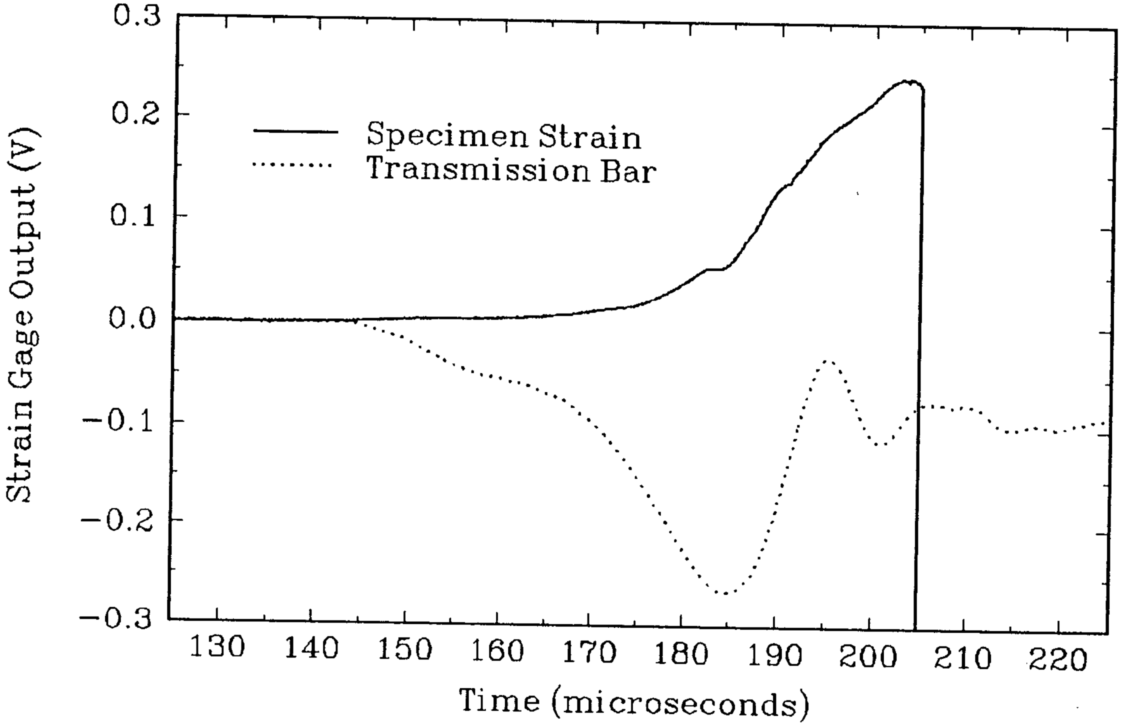

Fig.5. Dynamic specimen strain and transmission bar signals in an experiment with a confined Macor specimen.

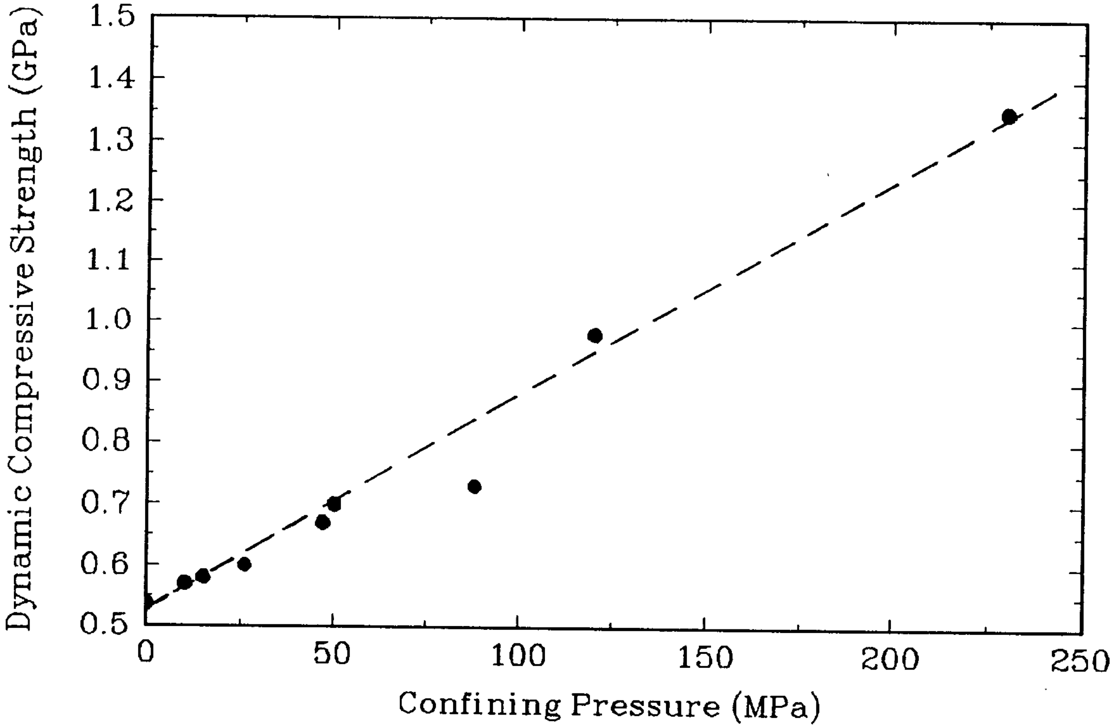

Fig.6. Variation of dynamic compressive strength of Macor as a function of lateral confinement.

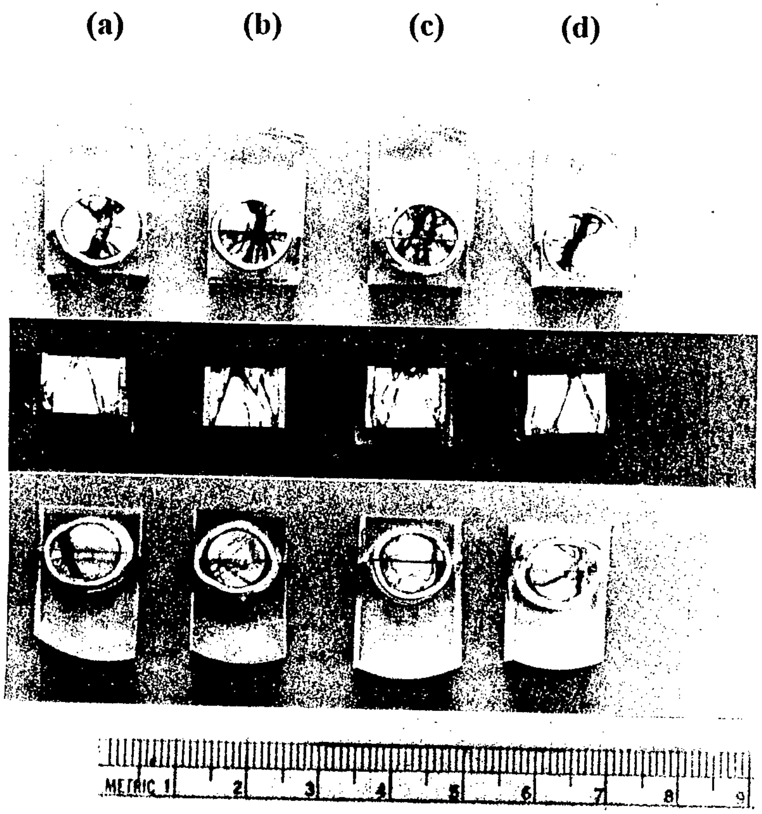

Fig. 7 . Recovered Macor specimens from quasi-static experiments.

Sleeves: (a) 6061 Al (σ_T=26 MPa), (b) brass (σ_T=47 MPa),

(c) 2024 Al (σ_T=50 MPa), and (d) 303 stainless steel(σ_T=88 MPa).

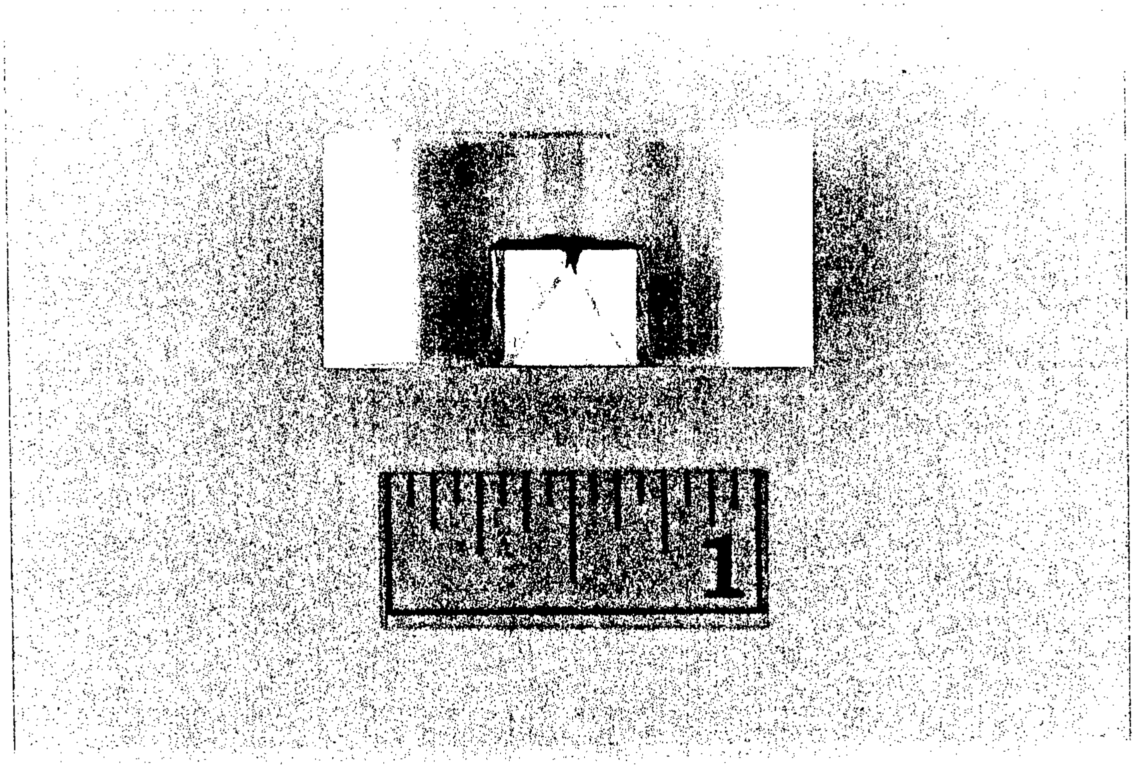

Fig. 8. A typical axial cross section of a Macor specimen with confinement recovered from a dynamic experiment.

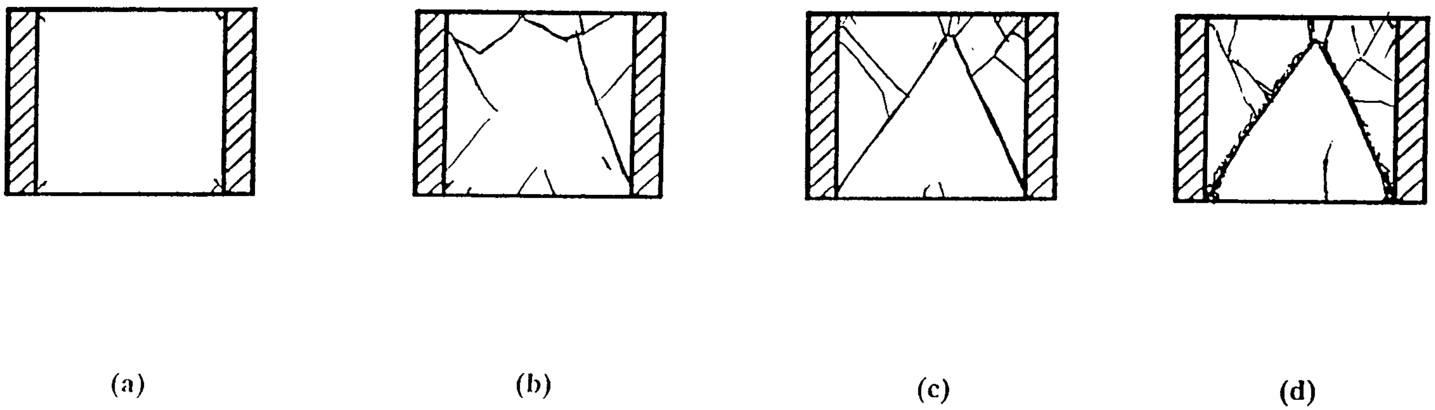

(a) (b) (c) (d)

Fig. 9. Schematic illustration of the process of the fault formation in the confined Macor specimen.

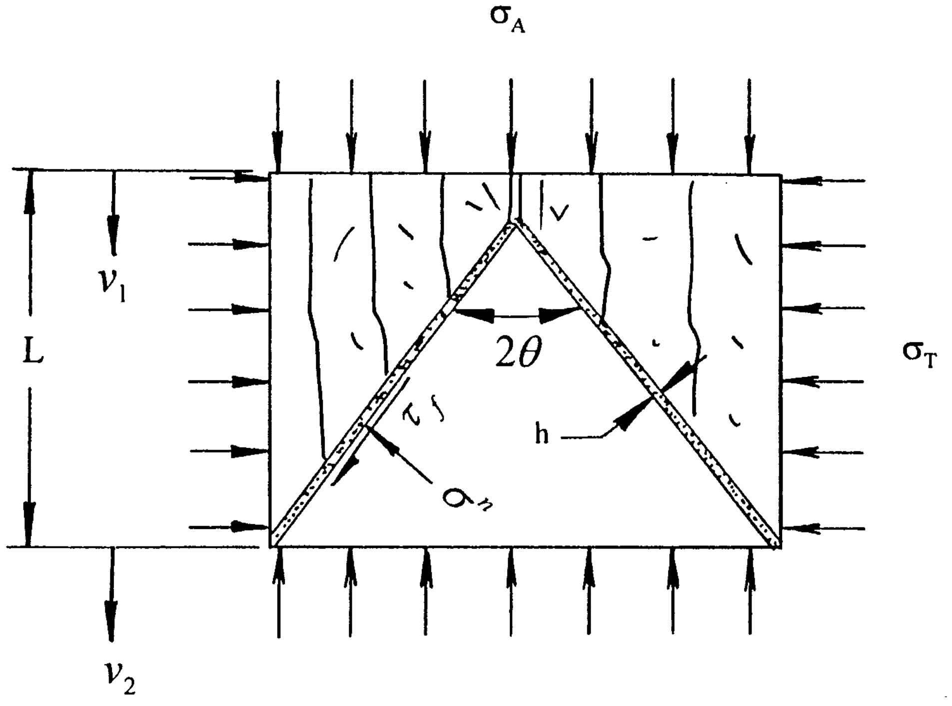

Fig. 10. A schematic illustration of the estimation of shear stress and shear strain rate in the conical rubble layer.

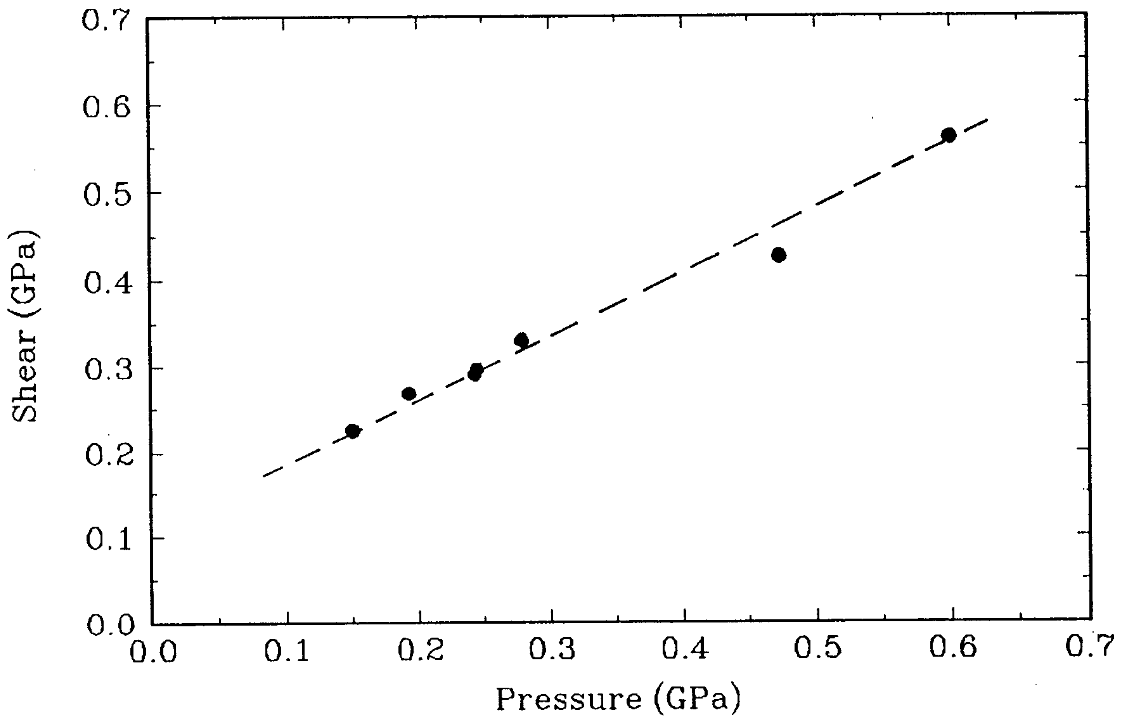

Fig.11. Failure surface of Macor for brittle failure.

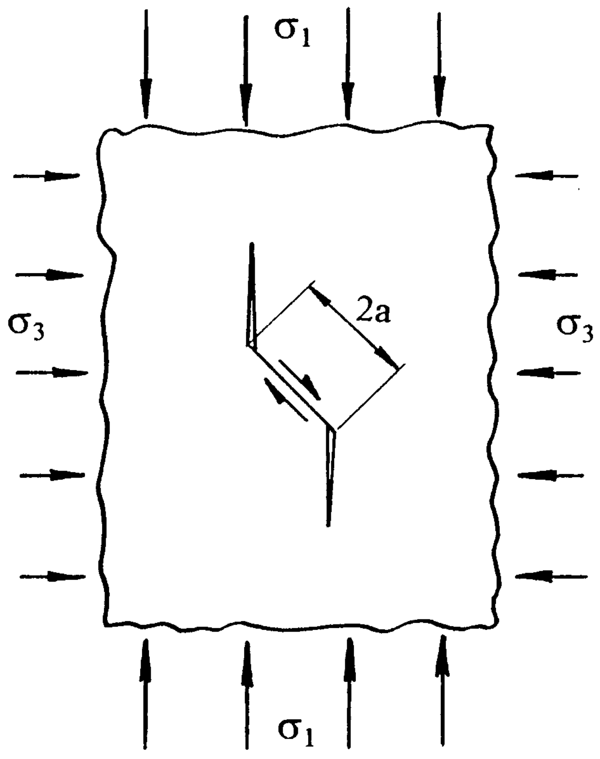

Fig. 12. A schematic illustration of a sliding crack model.

SECTION 2

Wave Propagation Through Fractured Solids

Introduction :

The aim of this study was to study the propagation of stress waves through cracked, brittle media. In order to readily control the introduction of cracks into the material it is desirable to choose a brittle material of low fracture strength. For this reason a low strength polymer glass, officially known as Break-Away glass, and colloquially as "Candy glass" in the movie industry was selected. While the strength characteristics are particularly desirable, it also turned out that very little was known about its physical and mechanical behavior. That lack of knowledge made it difficult to find a repeatable method for manufacturing specimens of desired shape and size as a prerequisite for setting up experiments to observe the wave propagation in this material. However, a series of studies have been accomplished by several students to understand the physical, chemical and mechanical properties of candy glass and to design an experimental set up. This report summarizes these studies and how they have led to the current progress.

Summary of Studies Performed on Break-Away Glass :

Infra Red absorption spectrum analyses determined that Break-Away glass is a polystyrene mixture with 3000 and 100,000 MW components. The mean of other properties measured are as follows.

ρ : Density = 1050 kg/m^3
σ_{max} : Maximum tensile strength = 5 Mpa
E : Young's modulus of elasticity = 3.88 Gpa
G : Shear modulus = 11.45 Gpa
K : Bulk modulus = 4.03 GPa
ν : Poisson's ratio = 0.34
c_n : Normal wave speed = 2382 m/s
c_s : Shear wave speed = 1174 m/s
T_g : Glass transition temperature = 64 °C
Material becomes very soft at 130-140 °C
T_b : Boiling temperature = 325 °C

The Dilatational wave speed (c_n) can be approximated as a function of temperature as

$c_n = 2400-2.9\ T \qquad 20 < T < 60\ (^{o}C)$

$\qquad\qquad\qquad\qquad = 2500-6.1\ T \qquad 60 < T < 120\ (^{o}C)$

The earliest studies[1,2,3] were directed at producing plate specimens. These specimens were to be subjected to short duration plane (plate) waves, before and after cracks of various arrangements were introduced. Several attempts to machine the material by milling, grinding, sanding as well as cutting with a hot knife did not produce satisfactory results, The main impediment was the extraordinarily low strength and brittle nature of the material.

Due to these difficulties in machining, attempts were made to cast the Break-Away glass in a mold, as was being done by previous graduate students for casting PMMA plates. However, early attempts did not yield satisfactory results, because the cast specimen would break into few pieces when cooled to less than 20 degrees C below the glass transition temperature, even with the use of mold release agents. During the closure of his studies, R. Teudt, the first student associated with this project, was able to cast break away material specimens with few cracks. He observed that since the specimens were breaking at around, 40 - 50 °C, just below the glass transition temperature (64 °C) as a result of the residual stress generated in the cool-down process and because the material adhered to the steel mold and its sides, as it solidified.

Current Studies :

During the past year, considerable progress has been made in (1) evolving a repeatable procedure that produces flawless specimens in a mold, (2) modifying a loading device for imparting controlled planar stress waves to plate specimens, (3) experimental technique, and (4) synchronization of the loading with the high speed camera.

1. Specimen preparation :

Once it was recognized that thermal stress build-up, together with the relatively low strength led to premature fracture of the specimens in the production process a method was devised to produce specimens of optical surface quality and without uncontrolled fractures.

This was achieved, basically, through first attaching Teflon tapes along the sides of the mold. In addition, these sides were loosened at around 75 °C at which temperature the material is still soft but is viscous enough not to flow out of the mold. Though this operation enlarged the number of unbroken specimens, it was a far from reliable method. In some trials the cast plate was removed from the mold at temperatures of 45 - 50 °C. However, the material was still soft at this temperature and stuck to the mold. After, several such trial attempts at varying the cooling rate, soaking and placing Teflon tapes in various locations, a repeatable procedure has been developed to produce plate specimens 12 x 12 x1/4 inches, and possessing an optically smooth surface over its central portion (3 x 4 inches) as described in the Appendix.

2. *Loading Device :*

Stress waves are generated in the plate specimens through a Lorentz stress wave generator. When a current is discharged through a double (multiply) folded copper strip the folds of this strip are forced apart due to the interaction of the current and associated magnetic fields in the "legs". In this application a capacitor bank discharges high current through a folded copper strip, when triggered through suitable high rate switches. When such a strip arrangement is placed on one edge of the plate and backed up with a sufficiently massive block or plate, a spacially uniform pressure is exerted on the plate. In the present case the capacitor bank is configured with the aid of specially designed inductor coils to yield a pressure pulse that rises to its maximum in about 15 microseconds and lasts for about 300. The copper strips are 0.23 inch wide and around four feet long. The arrangement is indicated in the figure below.

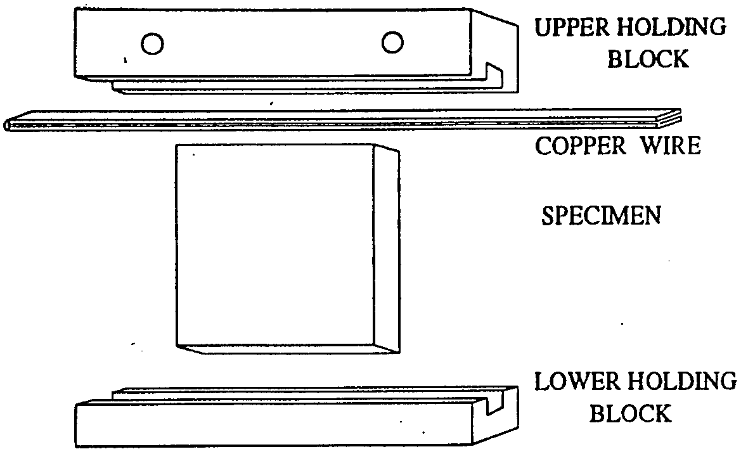

Fig. 13

Copper Strips :

When the copper strips are cut (by shearing) from a big sheet, they curl due to the internally generated residual stresses. The strips need to be annealed before use in the loading device. For this purpose, a slot or recess has been cut into two rectangular steel blocks; the folded strip is placed into the recesses and pressed between the blocks while being heated in an oven at 400 °F for three hours. When cool, the strip is stretched under a dead weight, thus further straightening it. Insulation tape is wrapped around the strip along its length. A normal 1/2 inch wide cellophane tape is used for this purpose. The strip then is folded (again) and placed in the holding slot in the back-up block of the loading device.

Capacitor Bank :

The stress generated by the copper wire when a current (i) flowing through it can be written as

$$\sigma = \tfrac{1}{2}\mu\left(\tfrac{i}{w}\right)^2$$

where w is the width of the copper strip.

The current depends on the voltage setting in the capacitor bank, and hence the magnitude of the stress pulse can be controlled by the voltage controller through which the capacitor bank is charged.

$$\sigma \propto V^2$$

The current flowing through the strip upon discharge of the capacitors is measured by means of a Rogovski coil so that the stress pulse imparted to the specimen can be calculated.

3. *Experimental Technique :*

The propagation of waves is to be observed by means of Twymann-Green interferometry. Though this technique is sensitive to external disturbances, the resolution of plate-normal deformations is very high. An estimation of various strains in the specimen (for $E = 3.88$ GPa ; $\nu = 0.34$) for a plane stress situation is

$$\varepsilon_{11} = 228 * 10^{-12} \sigma_{11}$$
$$\varepsilon_{22} = 0$$
$$\varepsilon_{33} = -117 * 10^{-12} \sigma_{11}$$

These interpret into plate-normal displacements of about 2.23 μm for stresses on the order to 3.0 MPa

4. *Light Source, Optics and Camera :*

The experimental technique requires interference of light. Also, high speed photographs need to be recorded at a rate of a few microsecond intervals. Hence, the existing laser pulser at GALCIT along with a pulse generator is the ideal choice for the light source.

The Twymann-Green technique for the analysis of out-of-plane deformations has been used frequently at GALCIT in the past. However, due to the brief discontinuity in the use of the facility, the optics for the camera and experiment had been dismantled. The optics have been set up again with the kind assistance of Dr. Washabaugh. Some other changes were made to improve the field of view from 22 mm to 50 mm for our case. The details of the optics is still being improved to reduce the glare on the film track, which is believed to be caused by the partial optical reflections at various lens planes.

5. *Synchronization of Events (Electronics) :*

This is a dynamic experiment which lasts for only few hundred microseconds. Hence, the synchronization of the events, especially the opening of the shutter, the triggering of the capacitor bank and the pulsing of laser plays a crucial role in the success of the experiment. As a consequence, the delays in triggering of various instruments needed to be calibrated.

Camera :

Before triggering, the air turbine of the high speed camera is brought to steady rotation. At a pressure setting of 15 psi (maximum) in the camera pressure gage, it is rotating such as to give a framing time interval of 6.5 - 7 μs. At this speed, one can obtain 128 exposures of full 35 mm film size, exposed at 7 μs intervals. However, one can reduce the exposed area to a small but reasonable size (say 20 mm and some gap between exposures) to increase the framing rate. An image size of 20 mm (for the actual size of 50 mm) on 3200 TMAX KODAK film gives good resolution. For this purpose, the framing rate has been set at 4.5 µs interval. An exposure time of 10 ns per frame via the pulsed laser gives less than 0.1% shift (blur) on the film track. The film is exposed for 700 µs giving around 155 pictures. These numbers are actually fixed by the pulse generator (H-P) and the camera should be rotating at a sufficient speed to avoid picture overlapping.

Shutter :

A copal shutter is used to open and close the optical track to avoid picture overlapping. From the above mentioned numbers, one needs to have the shutter open for at least 700 µs. However, due to the unreliability of this shutter (which is mechanical with an electrical triggering) the shutter is left open for 1/30 sec. It has been observed from experience that any light leakage during this comparatively large time does not effect the film exposure quality significantly. There is a 5 millisecond delay in the opening of the shutter after triggering. This is very important to note, as the other events also need to be delayed by the same time or more.

Laser Pulsing :

The intensity of light from the laser source with the R-F generator follows the electrical signal input into it virtually simultaneously. A pulse generator is triggered around 5 ms after the copal shutter is triggered. The pulse generator (Rutherford model) gives out a single square pulse of 700 µs duration, which is used as a gate input to another pulse generator (Hewlett-Packard or HP model). The HP pulse generator generates pulses at 4.5 µs intervals of 10-15 ns width to the laser unit when the gate input is on, . Thus around 155 laser pulses of 10 - 15 ns duration each, at an interval of 4.5 µs are obtained.

Capacitor Bank :

Similar to the laser, the capacitor bank is also triggered around 5 ms after the copal shutter is triggered. The capacitor bank has a mercury switch which needs a 2.0KV signal for on-switching. Various intermediate voltage step-ups are used for this purpose. The mercury switch is triggered by a Thyratron (250V - 2.2KV), which is triggered by a relay generator (10 - 250 V), which in turn is triggered by a 10 Volt signal.

Current Status and Future Plans :

At present, a few trial runs have been made with intact specimens (i.e. with no cracks). In one of the trials, a wave front was captured in 3 frames, as can be seen in Fig.14b, Fig.14c and Fig.14d, followed by some disturbances which were not expected. These disturbances, as seen in Fig.14d, Fig.14e and Fig.14f, could be due to some unloading waves generated from the side corners of the specimen or could be reflected waves from the free end of the block holding the copper wire on the other side. Further, as mentioned earlier some glares are observed on the film track, which are believed to be formed due to partial reflections of lights at various surfaces. Further investigations are being made along these directions to establish a reliable experimental set up, which would make it easy to observe the interaction of waves with cracks in Break Away glass specimens.

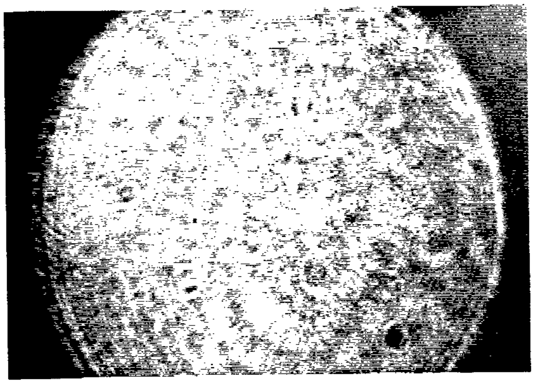

Fig 2a Before arrival of wave (t_0)

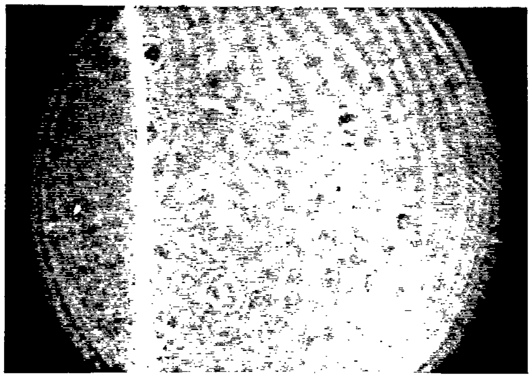

Fig 2b Wave near the right end ($t_0 + 6.5\ \mu s$)

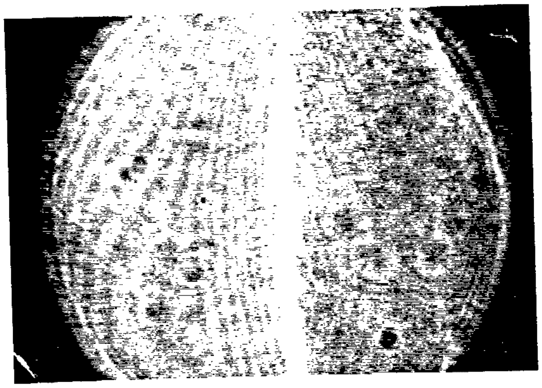

Fig 2c Wave at the center ($t_0 + 13\ \mu s$)

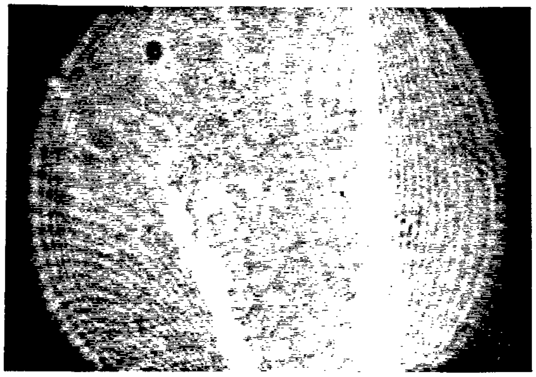

Fig 2d Wave near the left end, disturbances following ($t_0 + 19.5\ \mu s$)

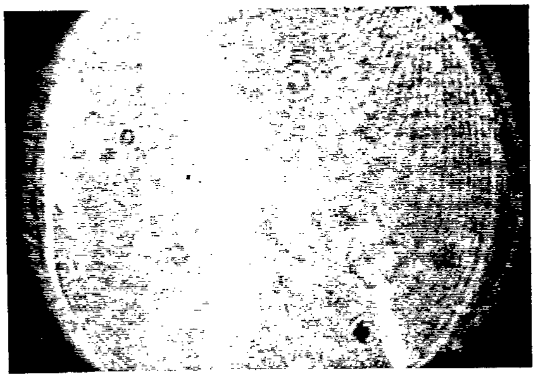

Fig 2e Wave not in view, disturbances following ($t_0 + 26 \mu s$)

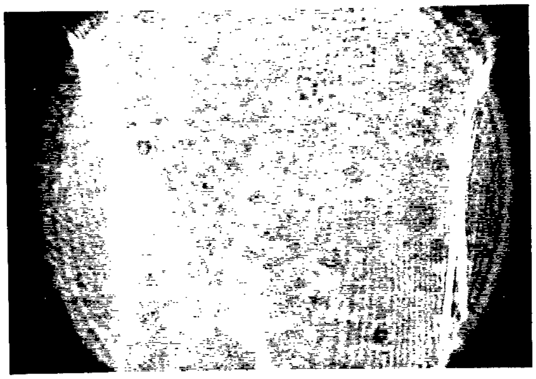

Fig 2f Wave not in view, disturbances following ($t_0 + 32.5\ \mu s$)

Fig. 14. Sequence of events at 6.5 μs intervals

SECTION 3

Shock Induced Gas-Producing Reactions

Shock-Induced Gas-Producing Reaction *

Many solid media, when subjected to impact-induced shock waves result in decomposition and gas production. We have studied gas reactions:

$$CaSO_4 + SiO_2 \rightarrow CaSiO_3 + SO_3 \uparrow \qquad (A)$$

$$CaSO_4 \rightarrow CaO + SO_2 \uparrow + \frac{1}{2} O_2 \uparrow \qquad (B)$$

Reaction (A) is of interest because of its lower incipient reaction temperature than reaction (B) (1200 K against 1450 K) based on Gibbs formation energy calculations, using thermodynamic data from Robie et al. [1979] (we assume ambient SO_2/SO_3 and O_2 partial pressures of 10^{-4} and 0.2 bar, respectively, as in the atmosphere).

Compared to theoretical calculations, we found the experimental degree of sulfate devolatilization for powdered samples (particle size was tens of microns) was $\sim 10^2$ times lower than predicted thermodynamically.

1. Reaction between Silica and Anhydrite :

Experimental parameters are listed in Table 4 (two shock experiments on anhydrite/SiO are listed and will be discussed later). The starting material was a mixture of silica (crystalline or amorphous, Alfa #13024 and 89709) and natural crystalline anhydrite powders and was pressed into the target container to initial densities of 60-85% of its Archimedian density. The average silica grain size was 4 μm and anhydrite grains were mostly between 30 and 100 μm. Equation-of-state constants for the mixture (Table 5) were calculated from the anhydrite data of Simakov et al. [1974] and the quartz data of Swegle et al. [1990] using the formulae of Boslough [1990]. Assuming uniform stress distribution, for a two-component system:

$$V = m_1 V_1 + m_2 V_2 \qquad (1)$$

$$K_{OS} = [(\upsilon_1 / K_{OS1}) + (\upsilon_2 / K_{OS2})]^{-1} \qquad (2)$$

$$K'_{OS} = K^2_{OS}[\upsilon_1(1+K'_{OS1})/K^2_{OS1} + \upsilon_2(1+K'_{OS2})/K^2_{OS2}] - 1 \qquad (3)$$

where m_1, V_i, υ_1, K_{OS1}, and K'_{OS1} are the components' mass fractions, specific volumes, initial volume fractions, bulk moduli and their pressure derivatives at zero pressure.

Table 4 Recovery experiments on anhydrite/silicate and anhydrite/SiO

Shot[a]	Sample	Molar ratio (anhydrite:silica)	Projectile	V_{proj} (km/s)	P_{peak} (GPa)
1106	Anhydrite/qtz	1:1	Ta	1.87	33.8
1107	Anhydrite/fused qtz	1:1	W	2.02	42.2
1108	Anhydrite/qtz	1:1	Ta	1.92	35.0
1109	Anhydrite/qtz	1:3.7	Ta	1.90(?)	42.3
1110	Anhydrite/qtz	3.0:1	Ta	1.94	32.5
1111	Anhydrite/qtz/Fe	1:1	Ta	1.89	34.3
1112	Anhydrite/qtz	1:1	Ta	1.88	34.1
917(40mm gun)	Anhydrite/qtz	1:1	Ta	1.59	27.4
923(40mm gun)	Anhydrite/qtz	1:1	Ta	1.77	31.5
1098	anhydrite/SiO	-	W	2.06	-
1099	Anhydrite/SiO	-	Ta	1.58	-

[a] On Caltech's 20 mm gun unless stated otherwise.

Table 5 Equation-of-state constants of anhydrite, silica and their mixtures

Material	ρ (g/cm^3)	K_{OS} (GPa)	K_{OS}'
Anhydrite (LPP)	2.97	38.5	6.0
Silica (HPP)	4.29	350	3.3
Mixture(1:1 molar)	3.28	48.7	7.6

Shock pressures, determined by the impedance-match method, range from 27.4 to 42.3 GPa. Five 20 mm shots and the two 40 mm shots (Table 4) all had a 1:1 molar ratio of anhydrite:silica. The initial porosity of the mixture varied between 17.2% (1106) and 40.0% (1108). Shot 1107 employed fused quaretz. The 40 mm shots were conducted to determine the effect of shock duration on the reaction but no reaction was seen in shot 917 and shot 923 was not recovered. Finally, shots 1109 and 1110 had anhydrite:silica molar ratios of 1:3.7 and 3.0:1. The samples recovered were analyzed with petrographic microscopy, scanning electron microscopy (SEM, instrument: Camscan Series 2 with Tracor Northern EDS detector TH-3/54-6901, operated at 13 kV) and X-ray diffraction (XRD, instrument: Scintag DMC-008, radiation source: Cu-$K_{\alpha 1}$). Compared with the original material, the changes exhibited in the 20 mm post-shock samples are quite similar (except shot 111, which will be described below): in agreement with previous research for silica becomes amorphous inspite of its original crystallinity, anhydrite is recovered as a crystalline phase. Although shock-induced mosaicism in the crystal grains was observed with cross-polarized light under the petrographic microscope, it appears unlikely that anhydrite recrystallized from a melt because no rounding of the grains was observed.

2. *Mixing of Sulfate with Silica :*

In shocked samples the boundary layer between calcium sulfate and silica is thicker than the cold-pressed edge. In the following we examine several possible mixing mechanisms:

Solid state diffusion:

The diffusion constants of H, ^{18}O and ^{30}Si atoms in quartz have been documented in Brady [1995]. At 800° C, they vary over a wide range, with H having the highest D (2.5 x 10^{-11} m^2/s) and ^{30}Si having the lowest D (1.3 x 10^{-21} m^2/s). In the time scale of our experiments, ~1 μs, the characteristic distance $\sqrt{Dt}$ ~10^{-8}-10^{-2} μm is much smaller than the observed reaction zone thickness.

Liquid state diffusion:

Rubie et al. [1995] directly measured oxygen self-diffusivity in $Na_2Si_4O_9$ melt up to 1825°C and between 4 and 10 GPa. The diffusion constant they reported ranges from 1.0 to 4.2 x 10^{-10} m^2/s, increasing with temperature and pressure. Si-O bond breaking is the basic process controlling both O self-diffusion in $Na_2Si_4O_9$ and $CaSO_4$ diffusion in silica melt, which is of present interest. It is possible to use these data to obtain an order of magnitude estimate of mixing time and length scales in the SiO_2 liquid. Again, in the 1 μs shock duration, the highest diffusivity (4.20 x 10^{-10} m^2/s) gives characteristic distance of 2 x 10^{-2} μm, which is still too small to account for a mixing layer 1-10 μm in size.

Rayleigh-Taylor instability:

Although initially crystalline quartz is amorphized during shock, we cannot conclude that it has been once molten because quartz can transform to diaplectic glass without melting [Hörz, 1968]. Since there is a strong constant in the strength of quartz and anhydrite (~1 GPa for quartz and ~0.1 GPa for anhydrite), we suggest the Rayleigh-Taylor instability as the third mixing mechanism.

Rayleigh-Taylor instability arises at interfaces between two materials of different strength when they are strongly accelerated or decelerated along a direction perpendicular to their planar interface. According to the theoretical model of Drucker [1975], when shock waves propagate from a stronger material into a weaker material the interface experiences alternating compressional and tensile stress, due to perturbations (bumps) on the surface of the material. When the stress difference exceeds the strength of the stronger material (σ_0), the bumps grow freely and instability occurs. Two important derivations of the theory are threshold perturbation amplitude:

$$h\frac{th}{0} = H(1+\pi/2)\ \sigma_0\ F/P \qquad (4)$$

and the dependence on time of instability growth above the threshold:

$$h - h_0^{th} = (h_0 - h_0^{th})\cosh \sqrt{\beta Pt/(\lambda\rho H)} \qquad (5)$$

where: H = the thickness of the material;
h_0 = the initial perturbation amplitude;
ρ = the density of the material;
P = shock pressure;
λ = the perturbation wavelength;
F = a geometric factor between 0.25 and 1; and
$\beta = \frac{16}{(4+\pi)} F \sim 2-8.$

A prominent feature of the theory is that the threshold is independent of wavelength λ. Experiments by Barnes et al. on aluminum and 304 stainless steel plates support the theoretical prediction [Barnes et al., 1980].

For our case, $\sigma_0 \approx 1$ GPa, $\rho = 2.65$ g/cm^3, P = 40 GPa, $\lambda \approx H \approx 4$ μm grain size, the threshold thickness perturbation calculated from Eq. (4) is ~0.4 μm, which is very reasonable. Above the threshold, growth is very fast: for an initial perturbation 10% above the threshold, Eq. (5) indicates that it takes a few nanoseconds to grow to sizes comparable to $\lambda/2$, after which the theory is no longer valid.

From the above discussion, only the Rayleigh-Taylor instability emerges as a plausible mixing mechanism.

References

1. Vapor Deposition of Aluminum on Brittle Polystyrene Plates, Richard Teudt and W.G. Knauss, *SM Report 93-39.*
2. Studies for Observing Stress Wave Propagation in Polystyrene, Richard Teudt and W.G. Knauss, *SM Report 93-20.*
3. Method for Casting Optically Flat (One Side) Brittle Polystyrene Plates, Richard Teudt and W.G. Knauss, *SM Report 93-30.*
4. J. F. Barnes, D. H. Janney, R. K. London, K. A. Meyer and D. H. Sharp, Further experimentation on Taylor instability in solids, J. Appl. Phys. 51, 4678-4679, 1980.
5. M. B. Boslough, A thermochemical model for shock-induced reactions (heat detonations) in solids, J. Chem. Phys. 92, 1839-1848, 1990.
6. D.C. Drucker, 'Taylor instability' of the surface of an elastic-plastic plate, Mechanics Today 5, 1975.
7. R. A. Robie, B. S. Hemingway and J. R. Fisher, Thermodynamic properties of minerals and related substances at 298.15K and 1 bar (105 Pascals) pressure and at higher temperatures, U.S. Geol. Surv. Bull. 1452, 1979.
8. D. C. Rubie, C. R. Ross II, M. R. Carroll and S. C. Elphick, Oxygen self-duffusion in $Na_2Si_4O_9$ liquid up to 10 GPa and estimation of high-pressure melt viscosities, Am. Mineral. 78, 574-582, 1993.
9. G. V. M. N. Simakov, N. M. Pavlovskiy, N. G. Kalashnikov and R. F. Trunin, Shock compressibility of twelve minerals, Izv. Phys. Solid Earth 8, 488-492, 1974.
10. J. W. Swegle, Irreversible phase-transitions and wave-propagation in silicate geologic materials, J. Appl. Phys. 68, 1563-1579, 1990.
11. Arrowood, R., and Lankford, J. (1987) Compressive fracture processes in an alumina-glass composite. *J. Mat. Sci.* **22**, 3737-3744.
12. Ashby, M. F. and Sammis, C. G. (1990) The damage mechanics of brittle solids in compression. *Pure and Appl. Geophys.* **133**, 489-521.
13. Blumenthal, W. R. and Gray, III, G. T. (1990) Characterization of shock- loaded aluminum-infiltrated boron carbide cermets. *Shock Compression of Condensed Matter--1989* (ed. S. C. Schmidt, J. N. Johnson and L. W. Davison), pp. 393-396. Elsevier Science Publishers.
14. Cai, H. D., Kalceff, M. A. S. and Lawn, B. R. (1994) Deformation and fracture of mica-containing glass-ceramics in Hertzian contacts. *J. Mat. Res.* **9**, 762-770.

15. Chen, W., Subhash, G. and Ravichandran, G. (1994) Evaluation of ceramic specimen geometries used in the split Hopkinson pressure bar. *DYMAT Journal* **1**, 193-210.

16. Chen, W., Ravichandran, G. and Ramesh, K. T. (1995) A single pulse loading technique using the split Hopkinson pressure bar. SM Report 95-12 Graduate Aeronautical Laboratories, California Institute of Technology, Pasadena, CA.

17. Chen, W. and Ravichandran, G., (1996) Static and dynamic compressive behavior of aluminum nitride under moderate confinement. *J. Am. Ceram. Soc.* **79**, 579-584.

18. Corning Incorporated (1992) Macor-machinable glass ceramic: safety and health issues. *Technical Bulletin, Macor-03*, Corning, New York.

19. Follansbee, P. S. (1985) The Hopkinson bar. *Mechanical Testing, Metals Handbook*, **8,** 9th edition, pp. 198-217, American Society for Metals, Metals Park, Ohio.

20. Grady, D. E. (1995) Dynamic properties of ceramic materials. Sandia Report SAND94-3266, Sandia National Laboratories, Albuquerque, NM.

Heard, H. C. and Cline, C. F. (1980) Mechanical behavior of polycrystalline BeO, Al_2O_3 and AlN at high pressure. *J. Mat. Sci.* **15**, 1889-1897.

21. Horii, H. and Nemat-Nasser, S. (1986) Brittle failure in compression: splitting, faulting and ductile-brittle transition, *Phil. Trans. Roy. Soc. London* **319**, 337-374.

22. Jaeger, J. C. and Cook, N. G. W. (1979) *Fundamentals of Rock Mechanics*. Chapman and Hall.

23. Klopp, R. W. and Shockey, D. A. (1991) The strength behavior of granulated silicon-carbide at high-strain rates and confining pressure. *J. Appl. Phys.* **70**, 7318-7326.

24. Kolsky, H. (1949) An investigation of the mechanical properties of materials at very high rates of loading. *Proc. Roy. Soc. London* **B62**, 676-700.

25. Lankford, J. (1977) Compressive strength and microplasticity in polycrystalline alumina. *J. Mat. Sci.* **12**, 791-796.

26. Lankford, J. (1993) Dynamic compressive failure of brittle materials under hydrostatic confinement. *Experimental Techniques in the Dynamics of Deformable Solids* (ed. K. T. Ramesh), pp. 1-10. AMD-Vol. 165, ASME, New York.

27. Lankford, J. (1994) Utilization of the split Hopkinson pressure bar under hydrostatic confining pressure to characterize the compressive behavior of ceramics and ceramic composites. *Mechanical Testing of Ceramics and*

Ceramic Composites (ed. A. Gilat), pp. 1-12. AMD-Vol. 197, ASME, New York.

28. Nemat-Nasser, S., Isaacs, J. B. and Starrett, J. E. (1991) Hopkinson techniques for dynamic recovery experiments. *Proc. Roy. Soc. Lond.* **A435,** 371-391.
29. Olsson, W. A. and Forrestal, M. J. (1994) Sandia National Laboratories, Albuquerque, NM, work in progress.
30. Raiser, G. and Clifton, R. J. (1993) High-strain rate deformation and damage in ceramic materials. *J. Eng. Mat.* **115**, 292-299.
31. Ravichandran, G. and Chen, W. (1991) Dynamic failure of brittle materials under uniaxial compression. *Experiments in Micromechanics of Fracture Resistant Materials* (ed. K.-S. Kim), pp. 85-90. AMD-Vol. 130, ASME, New York.
32. Ravichandran, G. and Subhash, G. (1994) Critical appraisal of limiting strain rates for compression testing of ceramics in a split Hopkinson pressure bar. *J. Am. Ceram. Soc.* **77**, 263-267.
33. Sairam, S. and Clifton, R. J. (1994) Pressure-shear impact investigation of dynamic fragmentation and flow of ceramics. *Mechanical Testing of Ceramics and Ceramic Composites* (ed. A Gilat), pp. 23-40. AMD-Vol. 197, ASME, New York.
34. F. Hörz, Statistical measurements of deformation structures and refractive indices in experimentally shock loaded quartz, in: Shock Metamorphism of Natural Materials, B. M. French and N. M. Short, eds., pp. 243-254, Mono Book, Baltimore, 1968.
35. J. B. Brady, Diffusion data for silicate minerals, glasses, and liquids, in: Handbook of Physical Constants, T. J. Ahrens, ed., Am. Geophys. Union, 1995.

Appendix A

A repeatable procedure has been developed to cast the Break Away glass material into a 111/2 x 111/2 inch specimen of around 1/4 inch thickness.

(a) Mold Preparation

(i) Clean the mold and side bars using acetone and alcohol. Use a brass bar (brass being softer than steel, does not scratch the mold surface) to remove any material sticking to the surface. Surfaces should be cleaned with alcohol after using acetone, as Break Away glass is only partially soluble in acetone.

(ii) Apply 3/4 inch Teflon tapes to the side bars of the mold and along the edges of the bottom plate of the mold. This ultimately reduces stress built up in the specimen, during cooling.

(iii) Mask a 10cm x 8cm area at the center of the mold and apply a thin coat of Teflon based mold release agent over the remainder of the surface. The corresponding region in the specimen will be later coated with Aluminum vapor to attain a mirror like finish, and hence contamination with the mold release agent is not desirable.

(iv) Place one 111/4 X 111/4 X 1/4 (inch) plate, supplied by the manufacturer, on the mold and bolt the side bars to their respective places. The side bars and the sides of bottom mold are numbered to ensure high tolerance in dimensions.

(v) Place the mold with the break away glass plate in the oven and close the oven. Note that the top plate of the mold is not used. This is because Break Away glass is very brittle and when cooled down it will crack under the load of the top mold.

(b) Heating

After several trials, the following sequence was found to be optimal. Heat the mold with Break Away in it to 140 °C, let it soak at that temperature for around 14 hours. This lets any trapped air escape. When there are no visible air bubbles inside the material cool it to 75 °C, loosen the side bars so that the sides of specimen are no longer in contact with the bars. Then cool it down very slowly to room temperature. The detail has been described below and is programmed in the temperature controller.

File 1:

step 1 : Set temperature to 128 (123) °C in 1 hr 30 mins.
step 2 : Soak for 3 hrs.
step 3 : Set temperature to 142 (137) °C in 1 hr.
step 4 : Soak for 15 hrs.
step 5 : Set temperature to 128 (123) °C in 3 hr.
step 6 : Go to File 2.

File 2:

step 1 : Soak for 3 hrs.
step 2 : Set temperature to 82 (77) °C in 1 hr.
step 3 : Hold

The side bars are loosened at this point so that the sides of specimens do not stick to them. Then file 3 is run.

File 3:

step 1 : Set temperature to 72 (68) °C in 1 hr.
step 2 : Soak for 4 hrs.
step 3 : Set temperature to 58 (54) °C in 1 hr.
step 4 : Soak for 3 hrs.
step 5 : Set temperature to 49 (46) °C in 1 hr.
step 6 : Go to File 4

File 4:

step 1 : Soak for 2 hrs.
step 2 : Set temperature to 38 (36) °C in 1 hr.
step 3 : Set temperature to 30 (29) °C in 1 hr.
step 4 : End and hold

Note : the temperature given is for the upper plate of the oven and those given in brackets is for the lower plate of the oven.

(c) Aluminum Coating

At room temperature, the specimen is removed very carefully. At present, as trial experiments are being performed with intact plates, the plates are directly coated with Aluminum vapor in the existing coating facility at GALCIT.